J. Fluid Mech. (2003), *vol.* 477, *pp.* 129–173.
DOI: 10.1017/S0022112002003099 Printed in the United Kingdom

Green's functions for a source in a boundary layer: direct waves, channelled waves and diffracted waves

By TAKAO SUZUKI† AND SANJIVA K. LELE

Department of Aeronautics and Astronautics, Stanford University, Stanford, CA 94305, USA

(Received 29 January 2001 and in revised form 28 August 2002)

Green's functions for a source embedded in an isothermal transversely sheared boundary layer are compared with direct numerical simulation (DNS) at various frequencies and free-stream Mach numbers. The procedures developed for a mixing layer in Part 1 (Suzuki & Lele 2003) are applied to derive the low- and high-frequency Green's functions for direct waves, i.e. the third-order convective wave equation is solved using asymptotic matching. In addition, channelled waves propagating downstream along the wall are analysed using the normal mode decomposition. By introducing an adjoint operator of the convective wave equation with a mixed-type boundary condition on the wall, the corresponding Hilbert space is defined and eigenfunctions of channelled waves are normalized. Furthermore, diffracted waves in the shadow zone are formulated in the high-frequency limit. These theoretical predictions are compared with numerical simulations in two dimensions: DNS are performed based on the full Navier–Stokes equations (the ratios between the acoustic wavelength and the boundary layer thickness are $\lambda/\delta_{BL} = 4.0, 1.0$, and 0.25 at a free-stream Mach number of $M_\infty = 0.8$; and $\lambda/\delta_{BL} = 1.0$ at $M_\infty = 0.3$ and 1.2). The DNS results generally agree with the theories: the pressure amplitudes of direct waves and diffracted waves follow the high-frequency limit with a reasonable degree of accuracy in the intermediate- and high-frequency cases ($\lambda/\delta_{BL} = 1.0$ and 0.25). The DNS results for channelled waves also agree with the theoretical predictions fairly well. In addition, the acoustic impedance on the wall under a strongly sheared viscous boundary layer is derived asymptotically based on the modal analysis.

1. Introduction

When sound is generated in a region in which the mean velocity is strongly sheared, its radiation pattern becomes highly directional due to refraction (see figure 1). Assuming the mean flow to be isothermal and purely transversely sheared in two dimensions, two types of flow geometries are studied in this series of papers. In Part 1 (Suzuki & Lele 2003), sound from a mixing layer is analysed, while in this paper sound from a boundary layer is analysed. When the source is embedded in a boundary layer with a moderate free-stream Mach number, the interaction with a wall causes various complex phenomena as well as simple refraction. Such a situation can arise in many practical aero-acoustic problems, for example the noise from a turbulent boundary layer at a finite Mach number on an airfoil (Ffowcs Williams &

† Present address: California Institute of Technology, Division of Engineering and Applied Science, Pasadena, CA 91125, USA.

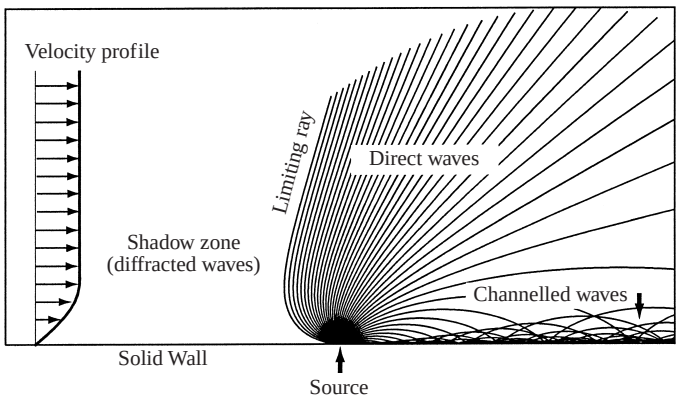

FIGURE 1. Schematic of ray trajectories from a point source in a boundary layer.

Hall 1970) or in a high-speed channel flow (Coleman, Kim, & Moser 1995; Goldstein & Leib 2000), the noise from a jet impinging on a flat plate (Powell 1991; Shen & Meecham 1993) or from jet–flap interaction (Ramakrishnan 1980), and so on.

In previous theoretical studies, the noise levels have been estimated assuming low free-stream Mach numbers (Curle 1955; Powell 1960; Howe 1979); accordingly, Lighthill's acoustic analogy (Lighthill 1952) has been extensively used. However, as the Mach number increases, refraction due to the shear flow in combination with the wall boundary needs to be taken into account. Strong refraction results in highly directional radiation patterns (see figure 1); in particular, at high-frequencies intensity becomes peaked at the 'critical angle'. Beyond this angle, there exists a region upstream of the source which direct waves cannot reach, referred to as a 'shadow zone'. Instead, diffracted waves occupy the shadow zone. On the other hand, downstream of the source, a large amount of acoustic energy trapped within a boundary layer propagates along the wall due to reflection as well as refraction (called a 'channelled wave' in this paper). Moreover, both diffracted waves and channelled waves interact with the non-slip wall on which the acoustic impedance could be non-zero. An understanding of all these phenomena is essential in analysing the sound from a boundary layer with a finite free-stream Mach number. However, these aspects have not been specifically studied in previous works.

One classical approach to understanding such a sound radiation problem is to seek fundamental acoustic solutions. This type of methodology, extensively explored in the 1960s and 1970s, can be now re-examined with the help of 'computational aero-acoustics' (CAA). Thus, the objective of this paper is to investigate Green's functions for a source in a boundary layer with a finite free-stream Mach number by comparing theoretical predictions with numerical simulations. This paper studies various wave phenomena relevant to a stationary point source, namely the sound radiation patterns of direct waves, channelled waves along the downstream wall, diffracted waves in the shadow zone, and related issues of the viscous wall boundary conditions.

As seen in studies of a mixing layer (such as Goldstein 1978, 1982), refraction must be taken into account when one estimates the sound level from a source embedded in a finite-Mach-number shear layer. Using the method studied in Part 1 (Suzuki & Lele 2003), asymptotic formulas for the radiation pattern of direct waves can be derived for a boundary layer. In the low-frequency limit, a vortex sheet model can

be applied (refer to previous works by Beckemeyer 1974 and Ffowcs Williams & Purshouse 1981, particularly for a boundary layer), while in the high-frequency limit the approach taken by Goldstein (1982) (based on the mathematical method derived by Avila & Keller 1963) can be applied (similar approaches were studied by Balsa 1976, Durbin 1983, and others). In both cases the third-order convective wave equation (Pridmore-Brown 1958; Lilley 1974) is solved using asymptotic matching, and the far-field solutions can be explicitly formulated in two and three dimensions using the stationary phase method. From these asymptotic formulas, the radiation pattern is shown to be highly directional as the free-stream Mach number increases; namely the rays are concentrated near the critical angle, at which the amplitude becomes peaked. In addition, it is predicted that directional patterns are quite different for the low- and high-frequency limits. All such information is entirely missing in the studies based on a free-space Green's function.

In addition to the peak near the critical angle, large-amplitude waves propagating along the wall are observed downstream. When the initial grazing angle of a ray is lower than a certain threshold value, this ray cannot penetrate the free stream due to strong refraction; as a result, it propagates downstream, bouncing between the turning points and the solid wall. Accordingly, caustics are formed, in which multiple rays focus, and a considerable amount of energy is trapped within the boundary layer downstream. These strong waves may have a significant impact on the interior noise of aircraft (Kriegsmann & Reiss 1983; Abrahams & Kriegsmann 1994). Similar phenomena can be observed in ocean acoustics, referred to as 'channelling' or a 'wave guide', in which rays are trapped between the upper surface and the turning points created by the temperature gradient. This phenomenon has been exhaustively investigated using two approaches: geometrical acoustics to statistically estimate the amplitude using ray tube theory (Brekhovskikh & Lysanov 1982), and the normal mode decomposition (Ahluwalia & Keller 1977) equivalent to obtaining eigenfunctions. The latter approach, which is used here, can be also widely applied, such as to duct acoustics (Pridmore-Brown 1958; Swinbanks 1975; Mani 1980; Wang & Kassoy 1992). However, much care is required to normalize the eigenfunctions when the mean flow has an arbitrary velocity profile. In this study, by introducing an adjoint operator for the third-order convective wave equation with a mixed-type boundary condition, the corresponding Hilbert space is constructed and eigenfunctions are normalized for channelled waves. To define the inner product, the method developed by Salwen & Grosch (1981) for the Orr–Sommerfeld equation is modified for compressible (inviscid) flows. This formulation is potentially usable to estimate acoustic pressure disturbances downstream with knowledge of the turbulent spectrum upstream. Thus, for the study of interior noise (Wilby 1996), not only the direct pressure fluctuation on the wall (Howe & Shah 1996; Graham 1996), but also the contribution from channelled waves should be taken into account.

On the other hand, upstream of the source, diffracted waves occupy the shadow zone instead of direct waves. If the angle of the ray becomes nearly tangent to the wall, these waves are allowed to propagate along the wall and to successively depart toward the shadow zone. These diffracted waves are exponentially decaying with respect to the distance from the source. Diffracted waves of similar types were formulated for wave equations with a transversely-varying index in the context of general geometrical acoustics by Seckler & Keller (1959*a*, *b*). For the current study, in the presence of velocity gradient, the derivation is almost identical to theirs although the wavenumber is included in the corresponding refraction index. By following their procedure, diffracted waves in a boundary layer with a finite free-stream Mach

number are formulated in the high-frequency limit. This formula is also useful to characterize the acoustic impedance of the wall.

An additional important aspect of a boundary layer is the viscous effect. When the acoustic wavelength becomes equivalent to or shorter than the boundary layer thickness, the coupling of three aerodynamic modes – acoustic, vorticity and entropy – becomes significant on the wall; hence, the simple boundary condition, $\partial p/\partial n = 0$, can no longer be applied. In the past, appropriate mixed-type boundary conditions have been derived assuming the free-stream Mach number to be negligible (refer to Pierce 1989; Anderson & Vaidya 1991). At high free-stream Mach numbers, however, these formulas for the boundary conditions need to be modified: the velocity gradient of the mean flow must be taken into account.

In this paper, all these aspects, which are relevant to the sound from a boundary layer with a finite free-stream Mach number, are investigated based on both theories and numerical simulations. In two dimensions the full Navier–Stokes equations are solved using direct numerical simulation (DNS) for five cases ($\lambda/\delta_{BL} = 4.0, 1.0$ and 0.25 at $M_\infty = 0.8$; and $\lambda/\delta_{BL} = 1.0$ at $M_\infty = 0.3$ and 1.2). A stationary sound source is prescribed by highly localized forcing terms, which simulate a time-harmonic monopole-type source. The results show that the direct waves in the high- and intermediate-frequency cases ($\lambda/\delta_{BL} = 0.25$ and 1.0) agree with the high-frequency limit relatively well, while the low-frequency case ($\lambda/\delta_{BL} = 4.0$) shows that the peak amplitude appears beyond the critical angle. Moreover, the comparison between the theory and DNS indicates that the peak amplitude is over-estimated. Regarding channelled waves, the mode shapes and amplitudes obtained from DNS are successfully predicted by the eigenfunctions calculated using the mean velocity profile of the DNS. In the shadow zone, the analytical expressions for diffracted waves and the DNS results are compared in terms of pressure amplitude: it is observed that the analytical expression based on the Neumann boundary condition ($\partial p/\partial n = 0$) agrees fairly well except in the low-frequency case ($\lambda/\delta_{BL} = 4.0$). Thus, various aspects of the acoustic phenomena associated with refraction and interaction with the wall are systematically studied over a wide range of the source frequency and the free-stream Mach number.

The outline of this paper is as follows. In § 2, Green's functions for a source in a boundary layer are derived: the low- and high-frequency asymptotes of direct waves, the normal mode decomposition of channelled waves, and diffracted waves in the high-frequency limit are formulated. In addition, the acoustic impedance for a viscous wall under a finite free-stream Mach number is discussed. In § 3, the procedures for the numerical simulations are described. In § 4, the theoretical predictions and the numerical simulations are compared, and the results are discussed. In the last section, conclusions are presented.

2. Derivation of Green's functions

This section describes the solutions for a stationary monopole source in a boundary layer, namely Green's functions. The conditions of the mean flow are similar to Part 1 namely a transversely sheared flow with constant temperature is assumed. For the coordinate system, x is taken to be the flow direction, y to be the vertical direction, z to be the spanwise direction, and η to be the vertical source position (see figure 2). To non-dimensionalize the equations, the ambient acoustic wavelength (at $M = 0$) is taken to be the length scale and the ambient speed of sound to be the velocity scale. (Thus, the angular frequency ω is equivalent to 2π.) A non-dimensional length scale

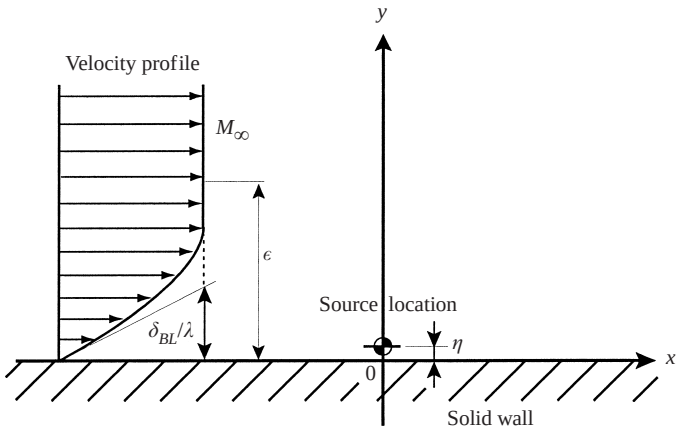

FIGURE 2. Coordinate system of a two-dimensional boundary layer.

of mean flow variation, ϵ, is defined so that it can fully cover any type of boundary layer thickness, such as the momentum thickness, the 99% velocity thickness, a length scale δ_{BL} defined later, etc. Since most of the derivation is analogous to the previous paper, only the differences are emphasized in this paper.

2.1. *Low frequency Green's function for direct waves*

To obtain Green's functions in a boundary layer, one can follow the procedures shown in § 2 of Part 1 (Suzuki & Lele 2003). The wave operator of the governing convective wave equation (Pridmore-Brown 1958) together with the monopole-type time-harmonic point source can be expressed as

$$\frac{\mathrm{D}}{\mathrm{D}t}\left[\frac{\mathrm{D}^2\Pi}{\mathrm{D}t^2}-\frac{\partial}{\partial x_j}\left(a^2\frac{\partial\Pi}{\partial x_j}\right)\right]+2\frac{\partial u_k}{\partial x_j}\frac{\partial}{\partial x_k}\left(a^2\frac{\partial\Pi}{\partial x_j}\right)=\frac{\mathrm{D}}{\mathrm{D}t}[\mathrm{e}^{-\mathrm{i}\omega t}\delta(x)\delta(y)], \tag{2.1}$$

where $\mathrm{D}/\mathrm{D}t\equiv\partial/\partial t+u_j\partial/\partial x_j$, a is the speed of sound, and $\Pi\equiv\gamma^{-1}\log(p/p_\infty)$ (γ denotes the specific heat ratio and p_∞ the ambient pressure). Note that (2.1) is expressed as the linearized form, the exact nonlinear equation for which was derived by Lilley (1974). Assuming that the mean velocity is transversely sheared, i.e. $u_j/a\equiv(M(y),0,0)$, one can take a Fourier transform of (2.1) in time and the flow direction; accordingly, the transformed convective wave operator becomes

$$\frac{\partial^2\hat{\Pi}}{\partial y^2}-2\frac{\bar{n}'}{\bar{n}}\frac{\partial\hat{\Pi}}{\partial y}+\omega^2(\bar{n}^2-\bar{k}^2)\hat{\Pi}=0, \tag{2.2}$$

where

$$\hat{\Pi}(\omega,k,y)=\frac{1}{(2\pi)^2}\int_{-\infty}^{\infty}\int_{-\infty}^{\infty}\Pi(t,x,y)\,\mathrm{e}^{\mathrm{i}\omega t}\mathrm{e}^{-\mathrm{i}kx}\,\mathrm{d}t\,\mathrm{d}x, \tag{2.3}$$

and $\bar{n}(y)\equiv 1-\bar{k}M(y)$, which corresponds to an 'index of refraction', and $\bar{k}$ is the normalized wavenumber in the x-direction. They are defined as $n\equiv\omega\bar{n}$ and $k\equiv\omega\bar{k}$, respectively.

Now, the only difference between a mixing layer and a boundary layer is the boundary condition. To generalize the problem, impose the third-kind (mixed-type) boundary condition:

$$\frac{\partial\hat{G}}{\partial y}-\mathrm{i}\omega\mathscr{Z}\hat{G}=0\quad\text{at}\quad y=0. \tag{2.4}$$

Here, the acoustic impedance $\mathscr{Z}$ can be complex and take any magnitude in this study ($0 \leqslant |\mathscr{Z}| \leqslant \infty$). Note that $\mathscr{Z}$ as defined here is normally called an 'acoustic admittance'. Although in many cases, particularly when the Reynolds number is relatively high and the acoustic frequency is not extremely high, one can assume $\mathscr{Z} = 0$ for a solid wall. However, in viscous flows the acoustic disturbances invoke other aero-dynamic modes involving vorticity and entropy disturbances; hence, $\mathscr{Z}$ takes a non-zero value. Section 2.5 (and Appendix C for the derivation) discusses the acoustic impedance for viscous boundary layers with a high free-stream Mach number. In the free stream ($y \to \infty$), the Sommerfeld radiation condition is imposed.

To derive the low-frequency Green's functions for direct waves, one can use asymptotic matching. The procedure is equivalent to using a vortex sheet across the source position (Beckemeyer 1974). The derivation given below may be more general than the one in Ffowcs Williams & Purshouse (1981). Here, the length scale ϵ is defined so that it satisfies $|(M(\epsilon) - M(\infty))/M(\infty)| \ll 1$, yet it is much smaller than the acoustic wavelength. First, consider the one-dimensional Green's function which is periodic in time and the flow direction, namely the solution for plane waves. Referring to the derivation in the mixing layer case (Suzuki & Lele 2003), one notices that only the outer solution on the lower side (A 13) in Part 1 must be replaced by (2.4). Moreover, because of the non-slip boundary condition, it is reasonable to assume $M(0) = 0$; hence, $\bar{n}_0 \equiv \bar{n}(0) = 1$. Accordingly, the one-dimensional Green's function for direct waves can be obtained as follows:

$$\hat{G}^{DR,low}_{(1)}(y) = \frac{\exp\left[\mathrm{i}\left(\omega\sqrt{\bar{n}_\infty^2 - \bar{k}^2}\,y - \tfrac{1}{2}\pi\right)\right]}{\omega\bar{n}_\eta^2\left(\sqrt{\bar{n}_\infty^2 - \bar{k}^2}/\bar{n}_\infty^2 - \mathscr{Z}\right)}, \tag{2.5}$$

where the superscript 'DR' stands for direct waves, and '*low*' for the low-frequency limit. The subscript (1) represents the dimension, the other subscripts denote the position in the y-coordinate, such as $\bar{n}_\eta \equiv \bar{n}(\eta)$, and the subscript ∞ denotes the free-stream quantity.

Similarly, to derive Green's function in two dimensions (for a line source), take an inverse Fourier transform of (2.5),

$$\hat{G}_{(2)}(x, y \mid \omega, 0, \eta) = \frac{1}{2\pi\mathrm{i}}\int_{-\infty}^{\infty} \frac{\exp\left[\mathrm{i}\omega\left(\bar{k}_x x + \sqrt{\bar{n}_\infty^2 - \bar{k}_x^2}\,y\right)\right]}{\bar{n}_\eta^2\left(\sqrt{\bar{n}_\infty^2 - \bar{k}_x^2}/\bar{n}_\infty^2 - \mathscr{Z}\right)}\,\mathrm{d}\bar{k}_x. \tag{2.6}$$

The arguments of $\hat{G}$ before the vertical bar denote the observer position, and the ones after denote the source frequency and the source position. The far-field asymptotic Green's function in two dimensions can be obtained using the stationary phase method as

$$\hat{G}^{DR,low}_{(2)}(r, \phi \mid \omega, 0, \eta)$$

$$\approx \frac{\sin\phi}{\sqrt{2\pi\omega r}(1 - M_\infty^2\sin^2\phi)^{3/4}} \frac{\exp\left[\mathrm{i}\left(\dfrac{-M_\infty\cos\phi + \sqrt{1 - M_\infty^2\sin^2\phi}}{1 - M_\infty^2}\omega r - \tfrac{3}{4}\pi\right)\right]}{(\bar{n}^\star_\eta)^2\left[\dfrac{(1 - M_\infty^2)^2\sin\phi\sqrt{1 - M_\infty^2\sin^2\phi}}{\left(\sqrt{1 - M_\infty^2\sin^2\phi} - M_\infty\cos\phi\right)^2} - \mathscr{Z}\right]}, \tag{2.7}$$

where $x \equiv r\cos\phi$ and $y \equiv r\sin\phi$. The stationary point is given by

$$\bar{k}_x^\star = \frac{1}{1-M_\infty^2}\left(-M_\infty + \frac{\cos\phi}{\sqrt{1-M_\infty^2\sin^2\phi}}\right). \tag{2.8}$$

Note that $\bar{n}_\eta^\star$ in (2.7) is evaluated at $\bar{k} = \bar{k}^\star$.

Finally, the three-dimensional asymptotic Green's function becomes

$$\begin{aligned}\hat{G}_{(3)}^{DR,low}&(r,\theta,\phi \mid \omega,0,\eta,0)\\ &\approx \frac{-1}{2\pi r}\frac{\sin\theta\sin\phi}{1-M_\infty^2(\cos^2\theta+\sin^2\theta\sin^2\phi)}\\ &\quad\times\frac{\exp\left[\mathrm{i}\dfrac{-M_\infty\sin\theta\cos\phi+\sqrt{1-M_\infty^2(\cos^2\theta+\sin^2\theta\sin^2\phi)}}{1-M_\infty^2}\omega r\right]}{(\bar{n}_\eta^\star)^2\left[\dfrac{(1-M_\infty^2)^2\sin\theta\sin\phi\sqrt{1-M_\infty^2(\cos^2\theta+\sin^2\theta\sin^2\phi)}}{\left(\sqrt{1-M_\infty^2(\cos^2\theta+\sin^2\theta\sin^2\phi)}-M_\infty\sin\theta\cos\phi\right)^2}-\mathscr{Z}\right]},\end{aligned} \tag{2.9}$$

where the stationary point is

$$\bar{k}_x^\star = \frac{1}{1-M_\infty^2}\left[-M_\infty + \frac{\sin\theta\cos\phi}{\sqrt{1-M_\infty^2(\cos^2\theta+\sin^2\theta\sin^2\phi)}}\right], \tag{2.10}$$

$$\bar{k}_z^\star = \frac{\cos\theta}{\sqrt{1-M_\infty^2(\cos^2\theta+\sin^2\theta\sin^2\phi)}}. \tag{2.11}$$

Likewise, $x \equiv r\sin\theta\cos\phi$, $y \equiv r\sin\theta\sin\phi$ and $z \equiv r\cos\theta$. Thus, the low-frequency Green's functions for direct waves in a boundary layer have been derived. Notice that when $\mathscr{Z} = 0$, (2.7) and (2.9) take finite values in $0^\circ \leqslant \phi \leqslant 180^\circ$, while when $\mathscr{Z} \neq 0$, they vanish at $\phi = 0^\circ$ and 180°. However, near $\phi = 180^\circ$ the next order terms in ϵ should be included when the leading-order terms in the denominator vanish. On the other hand, in the downstream direction, waves called 'channelled waves' propagate along the wall with large amplitude. These waves are discussed in § 2.3.

2.2. *High-frequency Green's function for direct waves*

In the high-frequency limit, the method introduced in § 2.2 of Suzuki & Lele (2003) (the original method is based on Avila & Keller 1963 and Goldstein 1982) can be applied. To modify it for a boundary layer, the mirror image technique is used. Take (2.15) in Part 1 to be an inhomogeneous solution (waves directly propagating from the source) and superpose a homogeneous solution (waves reflected from the wall). The summation can be expressed as follows:

$$\begin{aligned}\hat{G}_{(1)}(y) = A_1(y)\exp&\left[-\mathrm{i}\omega\int_\eta^y\sqrt{\bar{n}^2(y')-\bar{k}^2}\,\mathrm{d}y'\right]\\ &+A_2(y)\exp\left[\mathrm{i}\omega\int_\eta^y\sqrt{\bar{n}^2(y')-\bar{k}^2}\,\mathrm{d}y'\right]\quad(0\leqslant y<\eta).\end{aligned} \tag{2.12}$$

Substituting (2.12) into the mixed-type boundary condition (2.4) and evaluating it at $y = 0$, one can obtain the one-dimensional Green's function (plane wave solution) as

$$\hat{G}^{DR,high}_{(1)}(y) = \left[1 + \frac{\sqrt{1-\bar{k}^2} + \mathscr{Z}}{\sqrt{1-\bar{k}^2} - \mathscr{Z}} \exp\left(\mathrm{i}2\omega \int_0^\eta \sqrt{\bar{n}^2(y') - \bar{k}^2}\,\mathrm{d}y'\right)\right] \times \frac{\bar{n}_\infty \exp\left[\mathrm{i}\omega \int_\eta^y \sqrt{\bar{n}^2(y') - \bar{k}^2}\,\mathrm{d}y'\right]}{\mathrm{i}2\omega\bar{n}_\eta(\bar{n}_\eta^2 - \bar{k}^2)^{1/4}(\bar{n}_\infty^2 - \bar{k}^2)^{1/4}}. \tag{2.13}$$

Here, the superscript '*high*' stands for the high-frequency limit. At high-frequencies, interference occurs between waves directly propagating upward and those reflected once from the wall.

In the two- and three-dimensional cases, as shown in (2.16) of Part 1, one can approximate the stationary points $\bar{k}_x^\star$ by (2.8), or $\bar{k}_x^\star$ and $\bar{k}_z^\star$ by (2.10) and (2.11), respectively. By following the same procedure, the two- and three-dimensional high-frequency Green's functions for direct waves in the far field can be obtained as follows:

$$\hat{G}^{DR,high}_{(2)}(r,\phi \mid \omega,0,\eta) \approx \left[1 + \frac{\sqrt{1-(\bar{k}_x^\star)^2} + \mathscr{Z}}{\sqrt{1-(\bar{k}_x^\star)^2} - \mathscr{Z}} \exp\left(\mathrm{i}2\omega \int_0^\eta \sqrt{(\bar{n}^\star(y'))^2 - (\bar{k}_x^\star)^2}\,\mathrm{d}y'\right)\right] \times \frac{1}{2\sqrt{2\pi\omega r}} \frac{\sqrt{\sin\phi}\left(\sqrt{1 - M_\infty^2\sin^2\phi} - M_\infty\cos\phi\right)}{(1-M_\infty^2)(1-M_\infty^2\sin^2\phi)} \times \frac{\exp\left[-\mathrm{i}\left(\omega r\varphi(\bar{k}_x^\star) + \frac{3}{4}\pi\right)\right]}{\bar{n}_\eta^\star((\bar{n}_\eta^\star)^2 - (\bar{k}_x^\star)^2)^{1/4}}, \tag{2.14}$$

$$\hat{G}^{DR,high}_{(3)}(r,\theta,\phi \mid \omega,0,\eta,0) \approx \left[1 + \frac{\sqrt{1-(\bar{k}_x^\star)^2 - (\bar{k}_z^\star)^2} + \mathscr{Z}}{\sqrt{1-(\bar{k}_x^\star)^2 - (\bar{k}_z^\star)^2} - \mathscr{Z}} \times \exp\left(\mathrm{i}2\omega \int_0^\eta \sqrt{(\bar{n}^\star(y'))^2 - (\bar{k}_x^\star)^2 - (\bar{k}_z^\star)^2}\,\mathrm{d}y'\right)\right] \times \frac{-1}{4\pi r} \frac{\sqrt{\sin\theta\sin\phi}}{(1-M_\infty^2)[1 - M_\infty^2(\cos^2\theta + \sin^2\theta\sin^2\phi)]^{5/4}} \times \frac{\exp[-\mathrm{i}\omega r\varphi(\bar{k}_x^\star, \bar{k}_z^\star)]}{\bar{n}_\eta^\star((\bar{n}_\eta^\star)^2 - (\bar{k}_x^\star)^2 - (\bar{k}_z^\star)^2)^{1/4}}. \tag{2.15}$$

Here, $\varphi(\bar{k}_x) \equiv \int_\eta^y \sqrt{\bar{n}^2(y') - \bar{k}_x^2}\,\mathrm{d}y'/r$ in (2.14), and $\varphi(\bar{k}_x, \bar{k}_z)$ in (2.15) is similarly defined. Unlike the low-frequency limit, (2.14) and (2.15) vanish at $\phi = 0^\circ$ and 180° regardless of the value of $\mathscr{Z}$. However, along the wall, channelled waves propagate downstream at high-frequencies as well. In addition, the denominator $((\bar{n}_\eta^\star)^2 - (\bar{k}_x^\star)^2)^{1/4}$ or $((\bar{n}_\eta^\star)^2 - (\bar{k}_x^\star)^2 - (\bar{k}_z^\star)^2)^{1/4}$ can vanish at certain $\bar{k}_x$ and $\bar{k}_z$. Therefore, there is a region which direct waves cannot reach and also an angle beyond which rays cannot propagate in the far field. This region is referred to as a 'shadow zone', and the angle a 'critical angle'. The ray propagating along the boundary of the shadow zone is called

a 'limiting ray'. Refer to figure 1 for a typical sound radiation pattern. The formula for the critical angle is shown in Appendix A. In the shadow zone, diffracted waves propagate instead. Channelled waves and diffracted waves are discussed in § 2.3 and § 2.4, respectively.

2.3. *Channelled waves along the downstream wall*

When the initial grazing angle of the ray is lower than a certain threshold value, this ray propagates downstream, bouncing between the turning points and the solid wall. These waves are called 'channelled waves' in this paper. To analyse such waves, the incompressible viscous theory developed by Salwen & Grosch (1981) is modified to a compressible inviscid theory; subsequently, the normal mode decomposition (Ahluwalia & Keller 1977) is applied.

Consider a two-dimensional case (a line source). Suppose viscous dissipation throughout the medium and energy absorption on the wall are negligible. Consequently, one can express the acoustic field as a superposition of discrete and continuous modes of the governing equation: the transformed third-order convective wave operator in the present case. Here, the discrete modes are exponentially decaying in the vertical direction and called the 'normal modes' in this paper. Among these modes, ones with purely real wavenumbers in the flow directions correspond to channelled waves. By contrast, the continuous modes have oscillatory behaviour as $y \to \infty$, and are responsible for direct waves. These two types of mode shapes in the vertical direction (the discrete mode expressed by $A(y)$ and the continuous mode by $B(k_x, y)$) are called the 'eigenfunctions' here. Hence, the eigenfunction times $\mathrm{e}^{\mathrm{i}k_x x}$ becomes the normal mode for discrete cases. With these two types of modes, the acoustic pressure field is expressed as

$$\Pi_{(2)}(t,x,y) = \begin{cases} \mathrm{e}^{-\mathrm{i}\omega t}\left[\displaystyle\sum_{m_-=1}^{N_-} a_{m_-}A_{m_-}(y)\,\mathrm{e}^{\mathrm{i}k_{xm_-}x} + \int_{-\infty}^{0} B_-(k_x,y)\,\mathrm{e}^{\mathrm{i}k_x x}\,\mathrm{d}k_x\right] & \text{if} \quad x<0, \\ \mathrm{e}^{-\mathrm{i}\omega t}\left[\displaystyle\sum_{m_+=1}^{N_+} a_{m_+}A_{m_+}(y)\,\mathrm{e}^{\mathrm{i}k_{xm_+}x} + \int_{0}^{+\infty} B_+(k_x,y)\,\mathrm{e}^{\mathrm{i}k_x x}\,\mathrm{d}k_x\right] & \text{if} \quad x>0, \end{cases} \tag{2.16}$$

where $\mathrm{Re}[k_{xm_-}] < 0$ and $\mathrm{Re}[k_{xm_+}] > 0$. The wavenumber is expressed by k_x instead of $\omega\bar{k}_x$ for later convenience, and a_m is the complex coefficient of the mth normal mode. Note that in addition to these two modes, there exist so-called 'gust solutions' which are associated with the singularity due to the convective velocity (refer to Swinbanks 1975 or Möhring, Müller & Obermeier 1983 for details). These modes should be similarly treated by appropriately taking a branch cut. Among the discrete modes, the one which does not decay in the x-direction needs to be extracted. All $A_{m_\pm}(y)$ are the solutions to the transformed third-order convective wave operator:

$$\mathscr{L}A_m(y) \equiv (\omega - k_{xm}M)\frac{\mathrm{d}^2A_m}{\mathrm{d}y^2} + 2k_{xm}\frac{\mathrm{d}M}{\mathrm{d}y}\frac{\mathrm{d}A_m}{\mathrm{d}y} + (\omega - k_{xm}M)[(\omega - k_{xm}M)^2 - {k_{xm}}^2]A_m = 0, \tag{2.17}$$

with the boundary conditions given by

$$\frac{\mathrm{d}A_m}{\mathrm{d}y} = 0 \quad \text{at} \quad y = 0, \qquad A_m \to 0 \quad \text{as} \quad y \to \infty. \tag{2.18}$$

Likewise, $B(k_x, y)$ satisfies the transformed wave operator (2.17), but the second

boundary condition is replaced by

$$\frac{\mathrm{d}B}{\mathrm{d}y} \to \mathrm{i}\sqrt{(\omega - k_x M_\infty)^2 - k_x^2}\,B \quad \text{as} \quad y \to \infty. \tag{2.19}$$

For simplicity, the acoustic impedance is set to be $\mathscr{Z} = 0$: As seen later, this assumption is reasonable except for very large negative wavenumbers. Note that as described by Salwen & Grosch (1981), the number of normal modes should be finite in (2.16). In addition, k_{xm} can be complex; however, Mack (1984) reported that there are no inviscid modes which are exponentially growing in a Blasius boundary layer velocity profile with a moderate free-stream Mach number. In fact, only one mode with a purely real k_{xm_+} was found in each DNS case based on numerical integration of (2.17) with (2.18). On the other hand, all k_{xm_-} are complex in the upstream direction: these waves actually correspond to diffracted waves, which are described in next section. Now, substitute (2.16) into (2.1) to obtain

$$\begin{aligned}\mathscr{L}(\Pi) \equiv{}& \omega^3\Pi + \mathrm{i}3\omega^2 M\frac{\partial \Pi}{\partial x} + \omega(1-3M^2)\frac{\partial^2\Pi}{\partial x^2} + \mathrm{i}(M - M^3)\frac{\partial^3\Pi}{\partial x^3} \\ &+\omega\frac{\partial^2\Pi}{\partial y^2} + \mathrm{i}M\frac{\partial^3\Pi}{\partial x\partial y^2} - \mathrm{i}2\frac{\mathrm{d}M}{\mathrm{d}y}\frac{\partial^2\Pi}{\partial x\partial y} \\ ={}& -\left(\omega\delta(x) + \mathrm{i}M\frac{\partial\delta(x)}{\partial x}\right)\delta(y-\eta).\end{aligned} \tag{2.20}$$

Then take the second-order moment of (2.20) to obtain the jump condition, namely calculate $\int_{0_-}^{0_+} x^2\mathscr{L}(\Pi)\,\mathrm{d}x$. The result can be simplified as

$$\begin{aligned}&\sum_{m_+=1}^{N_+} a_{m_+}A_{m_+}(y) + \int_0^{+\infty} B_+(k_x, y)\,\mathrm{e}^{\mathrm{i}k_x x}\,\mathrm{d}k_x \\ &\quad - \sum_{m_-=1}^{N_-} a_{m_-}A_{m_-}(y) - \int_{-\infty}^{0} B_-(k_x, y)\,\mathrm{e}^{\mathrm{i}k_x x}\,\mathrm{d}k_x = 0.\end{aligned} \tag{2.21}$$

Likewise, the first- and zeroth-order moments yield

$$\begin{aligned}&\sum_{m_+=1}^{N_+} \mathrm{i}k_{xm_+}a_{m_+}A_{m_+}(y) + \int_0^{+\infty} \mathrm{i}k_x B_+(k_x, y)\,\mathrm{e}^{\mathrm{i}k_x x}\,\mathrm{d}k_x \\ &\quad - \sum_{m_-=1}^{N_-} \mathrm{i}k_{xm_-}a_{m_-}A_{m_-}(y) - \int_{-\infty}^{0} \mathrm{i}k_x B_-(k_x, y)\,\mathrm{e}^{\mathrm{i}k_x x}\,\mathrm{d}k_x = -\frac{1}{1-M^2(y)}\delta(y-\eta),\end{aligned} \tag{2.22}$$

$$\begin{aligned}&\sum_{m_+=1}^{N_+} -k_{xm_+}^2 a_{m_+}A_{m_+}(y) + \int_0^{+\infty} -k_x^2 B_+(k_x, y)\,\mathrm{e}^{\mathrm{i}k_x x}\,\mathrm{d}k_x - \sum_{m_-=1}^{N_-} -k_{xm_-}^2 a_{m_-}A_{m_-}(y) \\ &\quad - \int_{-\infty}^{0} -k_x^2 B_-(k_x, y)\,\mathrm{e}^{\mathrm{i}k_x x}\,\mathrm{d}k_x = \mathrm{i}\omega\frac{2M(y)}{(1-M^2(y))^2}\delta(y-\eta).\end{aligned} \tag{2.23}$$

To determine the coefficient a_m, the Hilbert space of these normal modes must be defined using an adjoint operator. This method is analogous to that of Salwen & Grosch

(1981) in which they discussed eigenfunction expansions for the Orr–Sommerfeld equation. Here, the adjoint convective wave operator can be written as

$$\mathscr{L}^{\dagger}A_n^{\dagger}(y) \equiv (\omega - k_{xn}M)\frac{\mathrm{d}^2A_n^{\dagger}}{\mathrm{d}y^2} - 4k_{xn}\frac{\mathrm{d}M}{\mathrm{d}y}\frac{\mathrm{d}A_n^{\dagger}}{\mathrm{d}y} + (\omega - k_{xn}M)\left[(\omega - k_{xn}M)^2 - k_{xn}^2 - \frac{3k_{xn}\,\mathrm{d}^2M/\mathrm{d}y^2}{\omega - k_{xn}M}\right]A_n^{\dagger} = 0, \qquad (2.24)$$

with the boundary conditions given by

$$\frac{\mathrm{d}A_n^{\dagger}}{\mathrm{d}y} = 3\frac{k_{xn}}{\omega}\frac{\mathrm{d}M}{\mathrm{d}y}A_n^{\dagger} \quad \text{at} \quad y = 0, \qquad A_n^{\dagger} \to 0 \quad \text{as} \quad y \to \infty. \qquad (2.25)$$

The adjoint eigenfunctions of the continuous mode, $B^{\dagger}(k_x, y)$, also satisfy (2.24), (2.25) at $y = 0$, and (2.19) as $y \to \infty$. Using the original wave operator (2.17) and the adjoint operator (2.24), the following conservation form can be derived:

$$\int_0^{\infty} \Pi_n^{\dagger}[\mathscr{L}(\omega_m, k_{xm})\Pi_m]\,\mathrm{d}y + \int_0^{\infty} \Pi_m[\mathscr{L}^{\dagger}(\omega_n, k_{xn})\Pi_n^{\dagger}]\,\mathrm{d}y + \left(\frac{\partial \Pi_m}{\partial t}\frac{\partial \Pi_n^{\dagger}}{\partial y} - 3\frac{\mathrm{d}M}{\mathrm{d}y}\frac{\partial \Pi_n^{\dagger}}{\partial x}\Pi_m\right)_{y=0} = \frac{\partial}{\partial t}\int_0^{\infty} J_t(\Pi_n^{\dagger}, \Pi_m)\,\mathrm{d}y + \frac{\partial}{\partial x}\int_0^{\infty} J_x(\Pi_n^{\dagger}, \Pi_m)\,\mathrm{d}y, \qquad (2.26)$$

where

$$\Pi_m = A_m(y)\,\mathrm{e}^{-\mathrm{i}(\omega_m t - k_{xm}x)}, \quad \Pi_n^{\dagger} = A_n^{\dagger}(y)\,\mathrm{e}^{\mathrm{i}(\omega_n t - k_{xn}x)}, \qquad (2.27)$$

$$J_t(\Pi_n^{\dagger}, \Pi_m) = \Pi_n^{\dagger}\frac{\partial^2 \Pi_m}{\partial t^2} + \Pi_m\frac{\partial^2 \Pi_n^{\dagger}}{\partial t^2} - \frac{\partial \Pi_n^{\dagger}}{\partial t}\frac{\partial \Pi_m}{\partial t} + 3M\left(\Pi_n^{\dagger}\frac{\partial^2 \Pi_m}{\partial t\partial x} + \Pi_m\frac{\partial^2 \Pi_n^{\dagger}}{\partial t\partial x}\right) + (1 - 3M^2)\frac{\partial \Pi_n^{\dagger}}{\partial x}\frac{\partial \Pi_m}{\partial x} - \Pi_n^{\dagger}\frac{\partial^2 \Pi_m}{\partial y^2} - \Pi_m\frac{\partial^2 \Pi_n^{\dagger}}{\partial y^2} - \frac{\partial \Pi_n^{\dagger}}{\partial y}\frac{\partial \Pi_m}{\partial y}, \qquad (2.28)$$

and

$$J_x(\Pi_n^{\dagger}, \Pi_m) = -3M\frac{\partial \Pi_n^{\dagger}}{\partial t}\frac{\partial \Pi_m}{\partial t} - (1 - 3M^2)\left(\Pi_n^{\dagger}\frac{\partial^2 \Pi_m}{\partial t\partial x} + \Pi_m\frac{\partial^2 \Pi_n^{\dagger}}{\partial t\partial x}\right) - (M - M^3)\left(\Pi_n^{\dagger}\frac{\partial^2 \Pi_m}{\partial x^2} + \Pi_m\frac{\partial^2 \Pi_n^{\dagger}}{\partial x^2} - \frac{\partial \Pi_n^{\dagger}}{\partial x}\frac{\partial \Pi_m}{\partial x}\right) - M\left(\Pi_n^{\dagger}\frac{\partial^2 \Pi_m}{\partial y^2} + \Pi_m\frac{\partial^2 \Pi_n^{\dagger}}{\partial y^2} + \frac{\partial \Pi_n^{\dagger}}{\partial y}\frac{\partial \Pi_m}{\partial y}\right) + \frac{\mathrm{d}M}{\mathrm{d}y}\left(2\Pi_n^{\dagger}\frac{\partial \Pi_m}{\partial y} - \Pi_m\frac{\partial \Pi_n^{\dagger}}{\partial y}\right). \qquad (2.29)$$

Here, only the mixed-type boundary conditions are retained. Since Π_m and $\Pi_n^{\dagger}$ are the solutions to (2.17) and (2.24), respectively, first two terms in (2.26) always vanish. In a spatial problem, since the frequency is common between Π_m and $\Pi_n^{\dagger}$ as long as

the boundary condition (2.25) is satisfied, only the last term on the right-hand side in (2.26) remains,

$$\frac{\partial}{\partial x}\int_0^\infty J_x\,\mathrm{d}y = -\mathrm{i}(k_{xn}-k_{xm})\int_0^\infty J_x\,\mathrm{d}y = 0. \tag{2.30}$$

Thus, when the wavenumbers of the normal modes are different, this particular 'inner-product' must be $\int_0^\infty J_x\,\mathrm{d}y = 0$, by which a bi-orthogonal system is constructed. This inner product can extract a discrete mode from an arbitrary superposition consisting of discrete and continuous modes and normalize the eigenfunction. Notice that this system is, however, invalid between two continuous modes because the boundary terms at $y \to \infty$ remain. In a temporal problem, however, the orthogonal condition does not simply become $(\omega_n - \omega_m)\int_0^\infty J_t\,\mathrm{d}y = 0$ in these expressions due to the mixed-type boundary condition. See Appendix B for the temporal problem.

In addition to the boundary layer problem, this method can be extended to two-dimensional duct geometries with an arbitrary mean velocity profile by imposing the boundary conditions on both sides (for example, $y = 0$ and $y = H$). Supposing the pressure fluctuation is dominated by the acoustic modes and the acoustic fluctuation is given at a certain cross-section, the problem can be decomposed into normal modes with appropriate coefficients using this inner product. Thus, the acoustic fields at other cross-sections are possibly predicted; however, when the magnitudes of the other modes, vorticity and entropy, become comparable to the acoustics mode in terms of pressure, this inner product cannot extract a certain acoustic mode. As another example, by knowing the source term, such as the velocity fluctuation in a turbulent boundary layer, the pressure disturbance on the downstream wall can be estimated, assuming that the boundary layer thickness is nearly constant. Furthermore, using this method, the receptivity of instability waves in a two-dimensional mixing layer can be estimated as described in § 2.5 of Part 1. Now, to determine the coefficient a_n, calculate the following 'inner product' using (2.21), (2.22), and (2.23):

$$J_x\left(\Pi_n^\dagger,\, \mathrm{e}^{-\mathrm{i}\omega t}\left[\sum_{m_+=1}^{N_+} a_{m_+}A_{m_+}\mathrm{e}^{\mathrm{i}k_{xm_+}x} + \int_0^{+\infty} B_+(k_x,y)\,\mathrm{e}^{\mathrm{i}k_x x}\,\mathrm{d}k_x\right.\right.$$
$$\left.\left. - \sum_{m_-=1}^{N_-} a_{m_-}A_{m_-}\mathrm{e}^{\mathrm{i}k_{xm_-}x} - \int_{-\infty}^{0} B_-(k_x,y)\,\mathrm{e}^{\mathrm{i}k_x x}\,\mathrm{d}k_x\right]\right) = J_x(\Pi_n^\dagger, a_n\Pi_n). \tag{2.31}$$

After some calculation, this yields

$$a_n^{CH} = \frac{-\mathrm{i}(\omega - k_{xn}M_\eta)A_n^\dagger(\eta)}{\displaystyle\int_0^\infty \hat{J}_x(\omega, k_{xn}, k_{xn}, A_n^\dagger, A_n)\,\mathrm{d}y}, \tag{2.32}$$

where

$$\begin{aligned}\hat{J}_x(\omega, k_{xn}, k_{xm}, A_n^\dagger, A_m) = {} & [-3\omega^2 M - \omega(k_{xn}+k_{xm})(1-3M^2) \\ & +(k_{xn}^2 + k_{xn}k_{xm} + k_{xm}^2)(M - M^3)]A_n^\dagger A_m \\ & -M\left(A_n^\dagger\frac{\mathrm{d}^2A_m}{\mathrm{d}y^2} + A_m\frac{\mathrm{d}^2A_n^\dagger}{\mathrm{d}y^2} + \frac{\mathrm{d}A_n^\dagger}{\mathrm{d}y}\frac{\mathrm{d}A_m}{\mathrm{d}y}\right) \\ & +\frac{\mathrm{d}M}{\mathrm{d}y}\left(2A_n^\dagger\frac{\mathrm{d}A_m}{\mathrm{d}y} - A_m\frac{\mathrm{d}A_n^\dagger}{\mathrm{d}y}\right).\end{aligned} \tag{2.33}$$

Here, the superscript 'CH' stands for channelled waves. $A_m(y)$ and $A_n^\dagger(y)$ are computed based on a compressible Blasius boundary layer profile, and the results are compared with the DNS data in § 4.2.

To extend this result to three dimensions, one needs to repeat the same procedure for each k_z and to take an inverse Fourier transform. Suppose $a_m(k_z)$ and $A_m(y, k_z)$ are obtained as functions of k_z. (Accordingly, the regular third-order wave operator (2.17) and its adjoint operator (2.24) with $-k_z^2$ added in the brackets of the third terms must be solved under the same boundary conditions.) Using these solutions, the acoustic field can be expressed as follows:

$$\Pi_{(3)}(t,x,y,z) = \frac{\mathrm{e}^{-\mathrm{i}\omega t}}{2\pi}\sum_{m=1}^{N}\left[\int_{-\infty}^{+\infty} a_m(k_z)A_m(y,k_z)\,\mathrm{e}^{\mathrm{i}[k_{xm}(k_z)x+k_z z]}\,\mathrm{d}k_z + \int_0^{+\infty}\int_{-\infty}^{+\infty} B(k_x,y,k_z)\,\mathrm{e}^{\mathrm{i}(k_x x+k_z z)}\,\mathrm{d}k_z\,\mathrm{d}k_x\right] \quad (x \geqslant 0_+), \tag{2.34}$$

and the coefficient $a_m^{CH}(k_z)$ can be similarly determined. Since the normal modes with a negative $\mathrm{Im}[k_{xm}]$ exponentially decay downstream, only the modes with a real k_{xm} (in three dimensions, families of these modes) dominate the sound within a boundary layer.

2.4. *Diffracted waves in the shadow zone*

It is seen from (2.8) (or (2.10) and (2.11) in three dimensions) that beyond the critical angle, no stationary point exists; therefore, instead of direct waves, diffracted waves propagate in the shadow zone. Part of the acoustic energy propagating upstream along the wall keeps departing toward the shadow zone. As described later, the ray trajectories of these diffracted waves have an identical shape to the limiting ray. At high-frequencies, Seckler & Keller (1959*a*, *b*) derived diffracted waves using two different methods, separation of variables and a contour integral, and obtained an identical result. Here, the method based on a contour integral is reviewed and modified for a boundary layer with a finite free-stream Mach number.

Start with (2.14) in Part 1, and neglect the lower-order term at high-frequencies,

$$\frac{\partial^2 \hat{G}^\bullet_{(1)}}{\partial y^2} + \omega^2[\bar{n}^2(y,\bar{k}) - \bar{k}^2]\hat{G}^\bullet_{(1)} = \frac{\delta(y-\eta)}{\bar{n}}. \tag{2.35}$$

Here, $\hat{G}^\bullet \equiv \hat{G}/\bar{n}$. Formulate the homogeneous solutions to (2.35) as follows:

$$\hat{G}^\bullet_{(1)}(y) = \begin{cases} g_1(y) = c_1 h_1(y) & \text{if} \quad y > \eta, \\ g_2(y) = c_3 h_1(y) + c_2 h_2(y) & \text{if} \quad 0 < y < \eta. \end{cases} \tag{2.36}$$

Note that h_1 indicates up-going waves and h_2 down-going waves. From the boundary condition on the wall (2.4), the coefficient c_3 can be determined as follows:

$$c_3 = -\frac{(\Upsilon h_2)_0}{(\Upsilon h_1)_0}c_2, \tag{2.37}$$

where $\Upsilon \equiv \partial/\partial y - \mathrm{i}\omega\mathscr{Z}^\bullet$ and $\mathscr{Z}^\bullet \equiv \mathscr{Z} + \mathrm{i}\bar{n}_0'/(\omega\bar{n}_0)$; however, the second term $\mathrm{i}\bar{n}_0'/(\omega\bar{n}_0)$ approaches zero in the high-frequency limit. To connect the solutions across the source position $y = \eta$, apply the asymptotic expansion used for the one-dimensional high-frequency Green's function (see Appendix A in Part 1); subsequently, (2.36) yields

$$\hat{G}^\bullet_{(1)}(y) = \frac{1}{\bar{n}_\eta(g_1'g_2 - g_2'g_1)_\eta}\begin{cases} g_2(\eta)g_1(y) & \text{if} \quad y > \eta, \\ g_1(\eta)g_2(y) & \text{if} \quad 0 \leqslant y < \eta. \end{cases} \tag{2.38}$$

Here, the Wronskian can be calculated as $(g_1'g_2 - g_2'g_1)_\eta = c_1c_2(h_1'h_2 - h_2'h_1)_\eta$. Knowing that h_1 and h_2 are the homogeneous solutions to (2.35), one can easily confirm that the Wronskian is constant with respect to y. Accordingly, evaluate the Wronskian on the wall $y = 0$, and rewrite (2.38) in terms of h_1 and h_2. After substituting it into the expression for an inverse Fourier transform, the equation for $y > 0$ yields

$$\hat{G}^{\bullet}_{(2)}(x, y|\omega, 0, \eta) = -\frac{\omega}{2\pi}\int_{-\infty}^{+\infty} \frac{[h_1(\eta)(\Upsilon h_2)_0 - h_2(\eta)(\Upsilon h_1)_0]h_1(y)\exp[\mathrm{i}\omega\bar{k}_x x]}{\bar{n}_\eta(h_1'h_2 - h_2'h_1)_0(\Upsilon h_1)_0}\,\mathrm{d}\bar{k}_x. \quad (2.39)$$

Now, to calculate (2.39), consider a contour integral. As shown by Seckler & Keller (1959*b*), only the term $(\Upsilon h_1)_0$ in the denominator contributes to a residue; hence, evaluate the rest of the terms at $\bar{k}_x^*$ satisfying $(\Upsilon h_1)_0 = 0$. Since h_1 and h_2 are linearly independent solutions propagating in opposite directions, it can be assumed that $h_1'(0) = \mathrm{i}\omega\mathscr{Z}^{\bullet}h_1(0)$ and $h_2'(0) = -\mathrm{i}\omega\mathscr{Z}^{\bullet}h_2(0)$. Consequently, (2.39) can be simplified as follows:

$$\begin{aligned}\hat{G}_{(2)}(x, y|\omega, 0, \eta) &\approx -\mathrm{i}\omega\frac{h_1^*(0)(\Upsilon h_2)_0^* h_1^*(\eta)h_1^*(y)\exp[\mathrm{i}\omega\bar{k}_x^* x]}{\bar{n}_\eta^*(h_1'h_2 - h_2'h_1)_0^*[h_1\partial(\Upsilon h_1)/\partial\bar{k}_x]_0^*} \\ &= -\mathrm{i}\frac{h_1^*(\eta)h_1^*(y)\exp[\mathrm{i}\omega\bar{k}_x^* x]}{[(\bar{n}_0^*)^2 - (\bar{k}_x^*)^2 - (\mathscr{Z}^{\bullet})^2]\bar{n}_\eta^*(h_1^*(0))^2(\partial y/\partial\bar{k}_x)_0^*}, \end{aligned} \quad (2.40)$$

where the quantities with the superscript $*$ are evaluated at $\bar{k}_x = \bar{k}_x^*$. To compute $\bar{k}_x^*$, approximate it using a second-order polynomial. Although the corresponding index $\bar{n}$ includes the wavenumber $\bar{k}_x$, the result becomes identical to (51) in Seckler & Keller (1959*b*) in the high-frequency limit,

$$\bar{k}_x^* \sim -\bar{n}_0 - \left[\frac{(\bar{n}_0')^2}{6\omega^2\bar{n}_0}\right]^{1/3} \mathrm{e}^{\mathrm{i}\pi/3}q_m, \quad (2.41)$$

where it is reasonable to assume $\bar{n}_0 = 1$ and $\bar{n}_0' \approx M'(0)$, and q_m is a discrete solution to the following equation:

$$\frac{A'(q_m)}{A(q_m)} = \mathrm{e}^{\mathrm{i}5\pi/6}\mathscr{Z}^{\bullet}\left(\frac{\omega}{6\bar{n}_0\bar{n}_0'}\right)^{1/3}. \quad (2.42)$$

Here, the Airy function is defined by (refer to Abramowitz & Stegun 1965)

$$A(q) \equiv \int_0^\infty \cos(t^3 - qt)\,\mathrm{d}t \quad \left(= \frac{\pi}{3^{1/3}}\mathrm{Ai}\left(-\frac{q}{3^{1/3}}\right)\right). \quad (2.43)$$

Note that to derive (2.42), only the leading terms in the high-frequency limit are retained. Likewise, in the high-frequency limit $(\partial y/\partial\bar{k}_x)_0^* = -1/\bar{n}_0^{'*}$ using (2.41). Furthermore, the asymptotic form of $h_1(y)$ for large $|y - \eta|$ is given by

$$h_1(y) = \left(\frac{3}{\pi\omega}\right)^{1/2}\frac{v^{1/2}}{(\bar{n}^2 - \bar{k}_x^2)^{1/4}}H_{1/3}^{(1)}(v) \approx \left(\frac{3}{\pi\omega}\right)^{1/2}\frac{\exp[\mathrm{i}(v - \frac{5}{12}\pi)]}{(\bar{n}^2 - \bar{k}_x^2)^{1/4}}, \quad (2.44)$$

where $v(y) = \omega\int_{y^*}^{y}\sqrt{\bar{n}^2(y', \bar{k}_x) - \bar{k}_x^2}\,\mathrm{d}y'$ and y^* denotes the turning point. Note that (2.41) is derived by setting $v(0) = -2q_m/3^{3/2}$. Consequently, substituting (2.41), (2.42)

and (2.44) into (2.40) yields

$$\hat{G}_{(2)}(x,y|\omega,0,\eta) \approx \frac{\pi e^{i\pi/3}}{46^{1/3}}\left[\frac{(\bar{n}_0^*)'}{\omega(\bar{n}_0^*)^2}\right]^{2/3} \times \frac{\exp\left[i\omega\left(\bar{k}_x^* x + \int_{y^*}^{\eta} + \int_{y^*}^{y}\sqrt{(\bar{n}^*)^2-(\bar{k}_x^*)^2}\,dy'\right)\right]}{[q_m A^2(q_m)+3A'^2(q_m)]\bar{n}_\eta^*((\bar{n}_\eta^*)^2/(\bar{n}_0^*)^2-1)^{1/4}((\bar{n}^*(y))^2/(\bar{n}_0^*)^2-1)^{1/4}}. \tag{2.45}$$

To simplify the phase part of (2.45), divide the interval of the integration at $y=0$. After some calculation using (2.41), it can be rewritten as

$$\begin{aligned}\int_{y^*}^{\eta} + \int_{y^*}^{y}\sqrt{(\bar{n}^*)^2-(\bar{k}_x^*)^2}\,dy' &\approx \int_0^{\eta} + \int_0^{y}\left[\sqrt{(\bar{n}^*)^2-(\bar{n}_0^*)^2} - \frac{e^{i\pi/3}}{6^{1/3}}\frac{q_m}{\bar{n}_0}\left[\frac{\bar{n}_0^*(\bar{n}_0^*)'}{\omega}\right]^{2/3}\frac{M^2\bar{n}_0+M-\bar{n}_0}{\sqrt{(\bar{n}^*)^2-(\bar{n}_0^*)^2}}\right]dy' \\ &\quad -\frac{1}{\omega}\frac{4}{3^{3/2}}q_m^{3/2}.\end{aligned} \tag{2.46}$$

Assuming both $|x|, |y| \gg \epsilon$, only the far-field solution is derived here. As seen in the stationary phase analysis, the rays become straight in the free stream. Therefore, the integration of the second term on the right-hand side of (2.46) can be approximated by

$$\int_0^{\eta} + \int_0^{y}\frac{M^2\bar{n}_0+M-\bar{n}_0}{\sqrt{(\bar{n}^*)^2-(\bar{n}_0^*)^2}}\,dy' \approx \frac{M_\infty^2+M_\infty-1}{\sqrt{M_\infty(M_\infty+2)}}y. \tag{2.47}$$

Notice that the interval of (2.46) corresponds to the limiting ray path and the term $\exp[i\omega\bar{k}_x^* x]$ in (2.45) provides the same coefficient as the second term of (2.46). Accordingly, the final expression becomes

$$\begin{aligned}&\hat{G}_{(2)}^{DF,high}(x,y|\omega,0,\eta) \\ &\approx \frac{\pi e^{i\pi/3}}{4\ 6^{1/3}}\left[\frac{(\bar{n}_0^*)'}{\omega(\bar{n}_0^*)^2}\right]^{2/3}\frac{\bar{n}_\infty^*\exp\left[i\omega\left(\bar{n}_0^*|x| + \int_0^{\eta} + \int_0^{y}\sqrt{(\bar{n}^*)^2-(\bar{n}_0^*)^2}\,dy'\right)\right]}{\bar{n}_\eta^*((\bar{n}_\eta^*)^2/(\bar{n}_0^*)^2-1)^{1/4}((\bar{n}_\infty^*)^2/(\bar{n}_0^*)^2-1)^{1/4}} \\ &\quad \times\sum_m \frac{\exp\left[\frac{\omega}{6^{1/3}\bar{n}_0^*}e^{i5/6\pi}\left[\frac{\bar{n}_0^*(\bar{n}_0^*)'}{\omega}\right]^{2/3}q_m\left|x-\frac{M_\infty^2+M_\infty-1}{\sqrt{M_\infty(M_\infty+2)}}y\right| - i\frac{4}{3^{3/2}}q_m^{3/2}\right]}{q_m A^2(q_m)+3A'^2(q_m)}.\end{aligned} \tag{2.48}$$

Again, the superscript '*DF*' stands for diffracted waves. To calculate (2.48), it is reasonable to substitute $\bar{k}_x^* \approx -1$. For extreme cases, $A(q_m)=0$ ($\omega^{1/3}|\mathscr{Z}^\bullet| \to \infty$), and $A'(q_m)=0$ ($\mathscr{Z}^\bullet=0$), discrete values of q_m are given in table 1 (see Abramowitz & Stegun 1965). Expression (2.48) including terms up to $m=5$ is compared with DNS in terms of amplitude later.

The three-dimensional expression (for a point source) can be similarly derived.

Zeros	q_1	q_2	q_3	q_4	q_5	q_6
$A(q_m)=0$	3.3721	5.8958	7.9620	9.7881	11.4574	13.0129
$A'(q_m)=0$	1.4693	4.6847	6.9518	8.8890	15.1835	17.8620

TABLE 1. Zeros of the Airy function.

Direct substitution into (62) of Seckler & Keller (1959*b*) yields

$$\hat{G}^{DF,high}_{(3)}(x,y|\omega,0,\eta)$$

$$\approx \frac{\pi^{1/2}\mathrm{e}^{\mathrm{i}\pi/12}}{2^{5/2}\,6^{1/3}}\left[\frac{(\bar{n}_0^*)'^4}{\omega(\bar{n}_0^*)^5}\right]^{1/6}\frac{\bar{n}_\infty^*\exp\left[\mathrm{i}\omega\left(\bar{n}_0^*\sqrt{x^2+z^2}+\int_0^\eta+\int_0^y\sqrt{(\bar{n}^*)^2-(\bar{n}_0^*)^2}\,\mathrm{d}y'\right)\right]}{\bar{n}_\eta^*\sqrt{x^2+z^2}((\bar{n}_\eta^*)^2/(\bar{n}_0^*)^2-1)^{1/4}((\bar{n}_\infty^*)^2/(\bar{n}_0^*)^2-1)^{1/4}}$$

$$\times\sum_m\frac{\exp\left[\dfrac{\omega}{6^{1/3}\bar{n}_0^*}\mathrm{e}^{\mathrm{i}5/6\pi}\left[\dfrac{\bar{n}_0^*(\bar{n}_0^*)'}{\omega}\right]^{2/3}q_m(\sqrt{x^2+z^2}-\sqrt{X^2+Z^2})-\mathrm{i}\dfrac{4}{3^{3/2}}q_m^{3/2}\right]}{q_mA^2(q_m)+3A'^2(q_m)},\tag{2.49}$$

where X and Z denote the coordinates at which a ray passing through the observer point departs from the wall. The exponential decay rate is the same as the two-dimensional case (2.48), but the cylindrical spreading rate is included in (2.49).

2.5. *Boundary conditions from the modal analysis*

In a viscous boundary layer, acoustic disturbances invoke other aero-dynamic disturbance modes, i.e. vorticity and entropy modes. In particular, when the acoustic wavelength is short, these three modes couple on the wall (see figure 3). Therefore, the superposition of these three modes must satisfy the non-slip as well as the no-penetration boundary conditions; accordingly, the simple boundary condition $\partial p/\partial n=0$ is no longer valid. Such a mode coupling was analysed using an asymptotic method by Kirchhoff (1868); consequently, appropriate viscous boundary conditions in a quiescent flow have been derived (the derivation is summarized in Pierce 1989); however, the effect of a steep velocity gradient near the wall was not taken into account. In this study, assuming that the mean velocity is transversely sheared, the viscous boundary conditions under a high free-stream Mach number are obtained. The derivation is given in Appendix C. These boundary conditions are valid when $Re_{ac}^{-1/2}\ll\min\{|\lambda/\delta_{BL}|,|\delta_{BL}/\lambda|\}$, which is satisfied in the DNS of this study (here, the Reynolds number Re_{ac} is based on the acoustic wavelength and the speed of sound). The resultant formulas for the acoustic impedances for an adiabatic and an isothermal wall are given by

$$\mathscr{Z}^{adb}_{(2)}\approx-\frac{1-\mathrm{i}}{2}\omega\bar{l}_{vor}\bar{k}_x^2\frac{1+\frac{1}{2}(1+\mathrm{i})\omega\Lambda\bar{l}_{ent}^2/\bar{l}_{vor}}{1+\frac{1}{2}(1+\mathrm{i})\omega\Lambda\bar{l}_{vor}(1-[(1-Pr)/2Pr]\bar{k}_x^2)},\tag{2.50}$$

$$\mathscr{Z}^{ist}_{(2)}\approx-\frac{1-\mathrm{i}}{2}\omega\frac{(\gamma-1)\bar{l}_{ent}(1+\frac{1}{2}(1+\mathrm{i})\omega\Lambda\bar{l}_{vor})+\bar{l}_{vor}\bar{k}_x^2(1+\frac{1}{2}(1+\mathrm{i})\omega\Lambda\bar{l}_{ent})}{1+\frac{1}{2}(1+\mathrm{i})\omega(\bar{l}_{vor}/\bar{k}_x)(2Pr/(1-Pr)-\bar{k}_x^2)(\mathrm{d}M/\mathrm{d}y)_{wall}}.\tag{2.51}$$

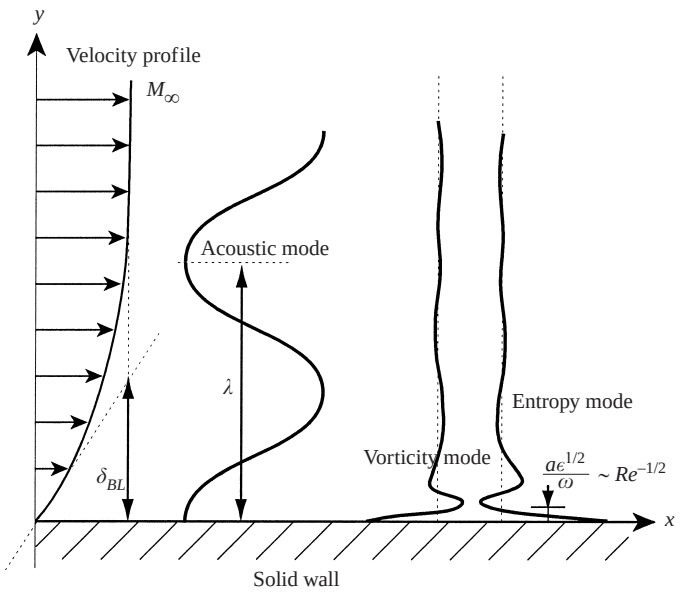

FIGURE 3. Schematic of length scales of the aero-dynamic modes in a viscous boundary layer. ϵ denotes the order of ϵ_μ or ϵ_κ defined after (C 5)–(C 7) in Appendix C.

Here, the superscripts '*adb*' and '*ist*' denote adiabatic and isothermal walls, respectively, and

$$\bar{l}_{vor} \equiv \sqrt{\frac{M_\infty}{\pi Re_{ac}}}, \quad \bar{l}_{ent} \equiv \sqrt{\frac{M_\infty}{\pi Pr Re_{ac}}}, \quad Re_{ac} \equiv a_\infty \lambda / \nu, \quad \Lambda \equiv \frac{2Pr}{1-Pr} \frac{1}{\omega \bar{k}_x} \left(\frac{\mathrm{d}M}{\mathrm{d}y} \right)_{wall}.$$

In the DNS the adiabatic boundary condition was imposed; accordingly, (2.50) was used for the theoretical prediction. In reality, as seen in figure 4, the effect of the mean velocity shear is negligible for a laminar boundary layer at a moderate free-stream Mach number. However, when the order of $M_\infty \bar{l}_{(vor/ent)} \lambda / \delta_{BL}$ approaches unity, namely $\omega \Lambda l_{(vor/ent)} \sim O(1)$, the effect of the shear may need to be taken into account. Note that the order of this parameter is $\omega \Lambda l_{(vor/ent)} \sim 0.1$ in the present DNS.

3. Numerical procedures

To compare the theoretical predictions with the numerical simulation, the full Navier–Stokes equations were explicitly solved using direct numerical simulation (DNS). For time marching, the standard fourth-order Runge–Kutta scheme was used. For spatial differencing, the sixth-order Padé scheme (Lele 1992) was used for the interior points. For the inflow and outflow, and the upper boundary points, lower-order (third and fourth) Padé schemes were used (Lele 1992). On the wall, the adiabatic boundary condition was imposed, with a third-order one-side-differencing scheme in the computational domain to solve pressure. The grid size, time step, etc. are shown in table 2. To prevent spurious reflection of acoustic waves from the computational boundaries, a so-called 'damping sponge' (Freund 1997) was used with the non-reflecting boundary conditions (Giles 1990). For the detailed numerical procedures and validation, refer to Suzuki (2001).

For the initial velocity field, the compressible Blasius boundary layer equation was solved using the Illingworth–Stewartson transformation. Based on this velocity field,

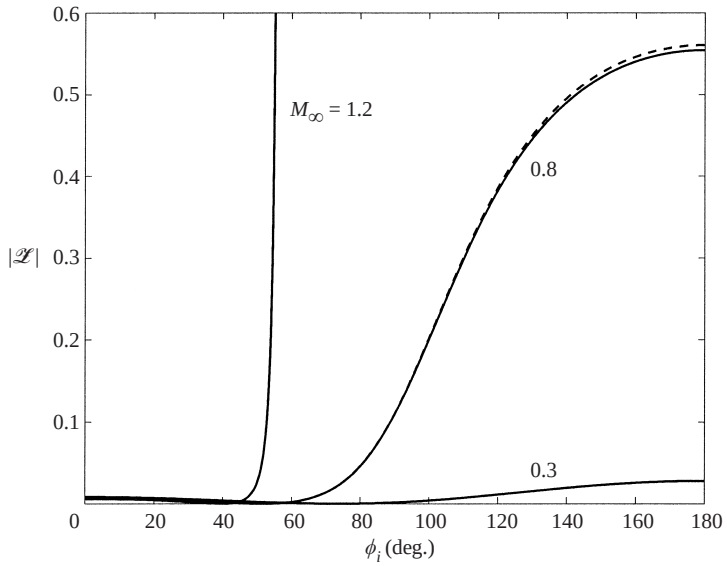

FIGURE 4. Angle dependence of the acoustic impedance for an adiabatic wall. Using (2.50), the acoustic impedance was computed for an adiabatic wall. The wavenumber $\bar{k}_x$ was calculated based on the angle of incidence ϕ_i using (2.8). Two curves at each Mach number almost overlap: – – –, $(\partial M/\partial y)_{wall} = 0$ (no mean flow; hence, $\Lambda = 0$); ——, $(\partial M/\partial y)_{wall} = M_\infty$ (shear flow).

temperature and density were computed using the Crocco–Busemann relation with the boundary conditions of $\rho_\infty = 1$, $T_\infty = 1$, and $(\partial T/\partial y)_{wall} = 0$. The Prandtl number was set to $Pr = 0.7$. The rest of the conditions are tabulated in table 2. Again, all quantities are normalized by the ambient acoustic wavelength λ (at $M = 0$) and the ambient speed of sound a_∞. (The Reynolds number is defined by $Re \equiv U_\infty \lambda / v_\infty$.) The length scale of the medium (called a 'boundary layer thickness' for convenience) is defined by

$$\delta_{BL} = \frac{U_\infty}{(\partial U/\partial y)_{wall}}, \tag{3.1}$$

at $x = 0$. For reference (at $M_\infty = 0.8$ and $Re = 1 \times 10^4$): the displacement thickness, $\delta_{dis} = 0.467\delta_{BL}$; the momentum thickness, $\delta_{mom} = 0.145\delta_{BL}$; and the 99% velocity thickness, $\delta_{99} = 1.66\delta_{BL}$. Note that the spreading rates of the boundary layer (defined by the slope of the $M(y) = M_\infty/2$ line) in the DNS were less than 0.1% for all cases.

Based on the initial velocity profile, ray trajectories were computed using the eikonal equation. Here, the temperature variation was ignored for simplicity. By the method of characteristics, the ODE system was integrated using the standard fourth-order Runge–Kutta scheme. Refer to Suzuki (2001) for the detailed procedures. A total of 60 rays was emitted in each case (every 6°), and the minimum time step was set to be $\Delta t = 1/800$ and exponentially stretched (less than a 3% increase for each time step).

To simulate a point source, the right-hand side of the Navier–Stokes equations was forced. Instead of imposing a delta function, a Gaussian-shaped source term whose narrow width limit becomes a delta function was imposed. With fine grid spacing near the source region, spurious high-frequency waves can be reduced using such source terms. By following the derivation of the third-order wave equation, it is deduced that the following forcing terms yield such a source:

$$\frac{\partial \rho}{\partial t} + \frac{\partial (\rho u_j)}{\partial x_j} = A_p(t)\gamma\rho F(t, x_1, x_2), \tag{3.2}$$

Case	Figure numbers	M_∞	$Re \equiv U_\infty \lambda/\nu_\infty$	λ/δ_{BL}	Ro	η
A	5, 6, 7, 22(*a*), 24(*a*)	0.8	4×10^4	4.0	10	0.020
B	8, 9, 10, 22(*b*), 24(*b*), 27	0.8	1×10^4	1.0	15	0.019
C	11, 12, 13, 20, 22(*c*), 23, 24(*c*)	0.8	2.5×10^4	0.25	28	0.031
D	14, 15, 16, 21, 22(*d*), 24(*d*)	0.3	0.375×10^4	1.0	15	0.019
E	17, 18, 19, 22(*e*), 24(*e*)	1.2	1.5×10^4	1.0	15	0.019

Cont.	Δt	(N_x, N_y)	$(\Delta x_{min}, \Delta y_{min})$	$(\Delta x_{max}, \Delta y_{max})$	(σ_x, σ_y)
A	1/1920	(480, 480)	(0.004, 0.000625)	(0.08, 0.05)	(0.00625, 0.00625)
B	1/800	(560, 400)	(0.008, 0.001500)	(0.08, 0.06)	(0.0150, 0.0025)
C	1/400	(580, 420)	(0.020, 0.002424)	(0.10, 0.08)	(0.0320, 0.0040)
D	1/800	(560, 400)	(0.008, 0.001500)	(0.08, 0.06)	(0.0150, 0.0025)
E	1/800	(560, 400)	(0.008, 0.001500)	(0.08, 0.06)	(0.0150, 0.0025)

TABLE 2. Parameters for the DNS.

$$\frac{\partial(\rho u_i)}{\partial t} + \frac{\partial(\rho u_i u_j + p\delta_{ij} + \tau_{ij})}{\partial x_j} = A_p(t)\gamma\rho u_i F(t, x_1, x_2), \tag{3.3}$$

$$\frac{\partial[\rho(e + \frac{1}{2}u_k^2)]}{\partial t} + \frac{\partial[\{\rho(e + \frac{1}{2}u_k^2) + p\}u_j + \tau_{jk}u_k + q_j]}{\partial x_j} = A_p(t)\gamma\rho(e + \tfrac{1}{2}u_k^2)F(t, x_1, x_2), \tag{3.4}$$

where

$$F(t, x_1, x_2) = \left[\frac{1}{\omega}\sin(\omega t) - \frac{(x_1 - x_{1p})u_1}{\omega^2 {\sigma_1}^2}\cos(\omega t)\right] \frac{\exp\left[-\sum_{j=1}^{2}\dfrac{(x_j - x_{jp})^2}{2{\sigma_j}^2}\right]}{2\pi\sigma_1\sigma_2}, \tag{3.5}$$

and (x_{1p}, x_{2p}) denotes the centre of the source. The form of the source terms is obtained by assuming that the mean velocity is purely vertically sheared and the magnitude of the local Mach number at the source position is small ($|M_\eta| \ll 1$). The width of the Gaussian shape was set to be $\sigma_2 \ll \sigma_1 \ll 1$ so that the source can be localized sufficiently close to the wall. Note that the first term inside the square brackets corresponds to the free-space Green's function, and the second term corresponds to the leading term of the mean flow correction. As a result, the corresponding source term of the convective wave equation yields

$$\frac{\mathrm{D}}{\mathrm{D}t}\left[\frac{\mathrm{D}^2\Pi}{\mathrm{D}t^2} - \frac{\partial}{\partial x_j}\left(a^2\frac{\partial\Pi}{\partial x_j}\right)\right] + 2\frac{\partial u_k}{\partial x_j}\frac{\partial}{\partial x_k}\left(a^2\frac{\partial\Pi}{\partial x_j}\right) = \frac{\mathrm{D}}{\mathrm{D}t}\left[(1 + O(M_\eta^2))\frac{A_p(t)\exp\left[-\sum\dfrac{(x_j - x_{jp})^2}{2{\sigma_j}^2}\right]}{2\pi\sigma_1\sigma_2}\cos(-\omega t)\right]. \tag{3.6}$$

Therefore, in the limit of $\sigma_1, \sigma_2 \to 0$, the right-hand side of (3.6) becomes a delta function, namely $(\mathrm{D}/\mathrm{D}t)[A_p\delta(\boldsymbol{x} - \boldsymbol{x}_p)\cos(-\omega t)]$. In computations the coefficient A_p was set to be $A_p(t) = 0.005[1 + \mathrm{erf}((t - t_1)/\sigma_t)]/2$, so that spurious high-frequency waves can be suppressed, where $\sigma_t = \pi/\omega$ and $t_1 = 2\pi/\omega$.

To measure the directivity of the pressure amplitude, 60 observer points were distributed on an upper half-circle nearly every 3°, centred at the source position with

a radius of approximately Ro. They were located on the grid points of the DNS, and the position errors defined by $|Ro - \sqrt{(x_1 - x_{1p})^2 + (x_2 - x_{2p})^2}|$ ($\sim O(\sqrt{\Delta x^2 + \Delta y^2})$) were corrected in the data processing. At these points, pressure profiles were recorded during two time periods after acoustic waves had arrived at all observer points. Subsequently, the pressure profile at each point was transformed into the frequency domain, and only the quantities at the forcing frequency were evaluated. In comparing these DNS results with the low- and high-frequency asymptotes of direct waves, corrections for viscous dissipation were included using an asymptotic formula (refer to Appendix D for the formula). Similarly, to compare the amplitude of diffracted waves, observer points were distributed along a straight line at $y = \eta$ in $x < 0$, and the same data-processing method was used.

To predict the mode shapes and amplitude of channelled waves, the Riccati forms of the third-order wave operator (2.17) and its adjoint operator (2.24) were solved using a shooting method based on a steady laminar boundary layer velocity profile obtained from DNS. The predictions are compared with the DNS results in which the channelled wave components are extracted. These numerical procedures are described in Appendix E in detail. Some problems in the post-processing will be discussed in § 4.2.

4. Results and discussion

4.1. *Overall sound radiation patterns and direct waves*

A total of five cases was simulated in DNS, and the dependence on the frequency and the Mach number was investigated. Parameters of each case are tabulated in table 2. In the following, the instantaneous pressure contours, the ray trajectories, and the corresponding pressure amplitudes are presented in polar plots, where the results of DNS are compared with the theoretical predictions for all three types of waves.

Figures 5–7 show the low-frequency case (Case A, see table 2). At lower angles (toward downstream) except on the wall, DNS and the asymptotic expressions for the direct waves agree very well. However, the amplitude peak appears somewhat beyond the critical angle, and this peak tends to shift toward the higher angle side as the distance increases. Moreover, the peak amplitude is obviously less than the prediction of the low-frequency limit. As seen in figure 7, the low-frequency limit predicts fairly large amplitude even beyond the critical angle. The DNS seems to show this transition although the result is still close to the high-frequency limit. Recall that in differentiating the phase part of the acoustic disturbance, a factor of 2π comes out, and the actual factor becomes comparable to unity in Case A ($2\pi\delta_{BL}/\lambda = 1.571$). Therefore, it is conceivable that sound radiation patterns do not follow the low-frequency limit except at extremely low-frequencies in real flows. Such a case was not performed in this study due to its high computational cost. Furthermore, note that the amplitude beyond the critical angle at low-frequencies is very sensitive to the acoustic impedance $\mathscr{Z}$ (see the denominator in (2.7)). As seen in figure 4, as the angle increases, the impedance substantially increases; hence, the amplitude at a higher angle tends to be suppressed. In reality, the next-order terms in ϵ would become more appreciable. In addition to direct waves, weak channelled waves and diffracted waves can be also observed in figure 5. These waves are discussed later.

Figures 8–10 show the intermediate-frequency case (Case B). As the frequency increases, the peak angle approaches the critical angle. The apparent peak angle of

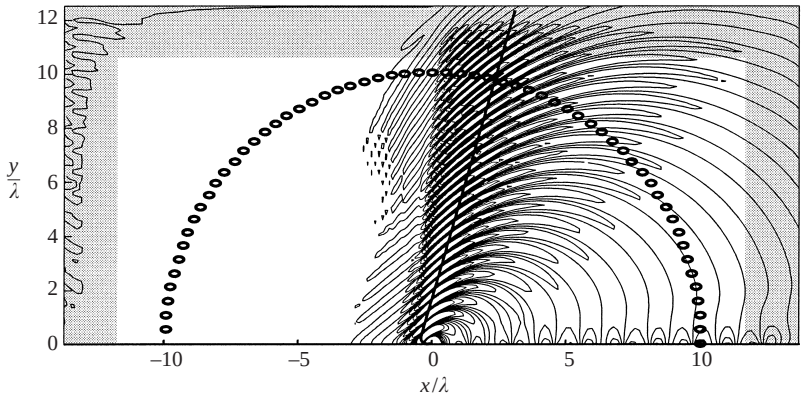

FIGURE 5. Pressure field at low-frequency, Case A ($M_\infty = 0.8$ and $\lambda/\delta_{BL} = 4.0$). Instantaneous pressure contours at time $t \approx 19$ are shown. Contour level: $0.999p_\infty$–$1.001p_\infty$ with intervals of $2.5 \times 10^{-4}p_\infty$. ——, the limiting ray, and ○, the points where the data were taken (at $Ro \approx 10\lambda$) to evaluate the amplitude (figure 7). Shaded region depicts the sponge boundary.

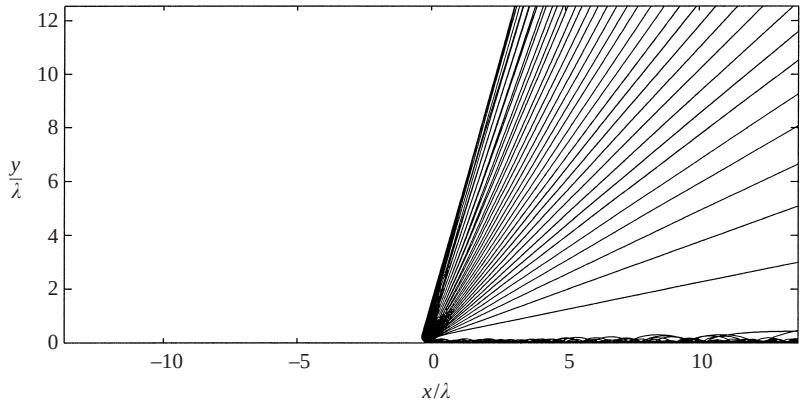

FIGURE 6. Ray trajectories at low-frequency, Case A. The eikonal equation was solved based on the initial velocity profile. The temperature variation was ignored.

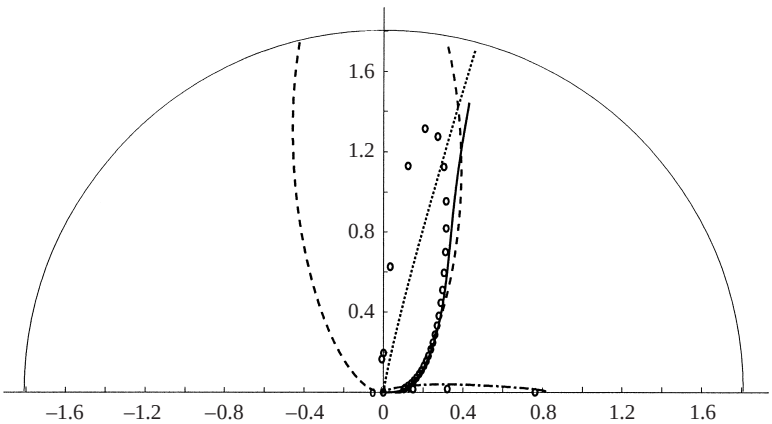

FIGURE 7. Pressure amplitude directivity at low-frequency, Case A. Pressure amplitude normalized by $\sqrt{Ro}$ (observer position $Ro \approx 10\lambda$) is shown in a polar plot: — — —, low-frequency limit of direct waves; ——, high-frequency limit of direct waves; ···, high-frequency limit of diffracted waves; — · — · —, channelled waves; ○, DNS result corresponding to figure 5. (After time $t = 17$, pressure histories were recorded during two time periods at 60 observer points.)

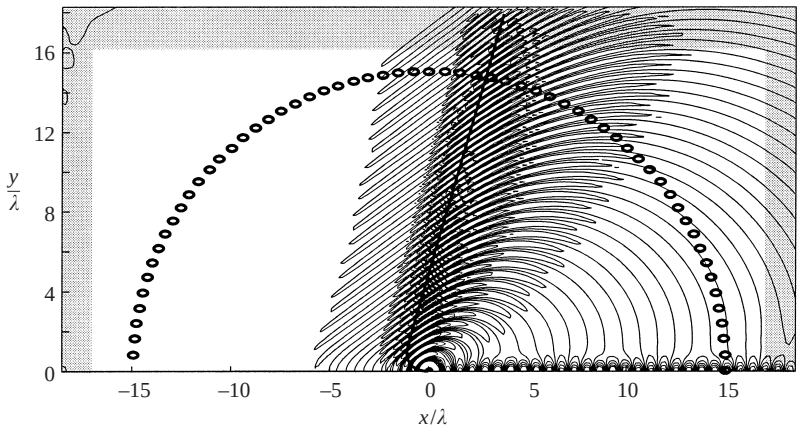

FIGURE 8. Pressure field at intermediate frequency, Case B ($M_\infty = 0.8$ and $\lambda/\delta_{BL} = 1.0$). Instantaneous pressure contours at time $t \approx 26$ are shown. Contour level and notation are the same as figure 5. The data were taken at $Ro \approx 15\lambda$ to evaluate the amplitude (figure 10).

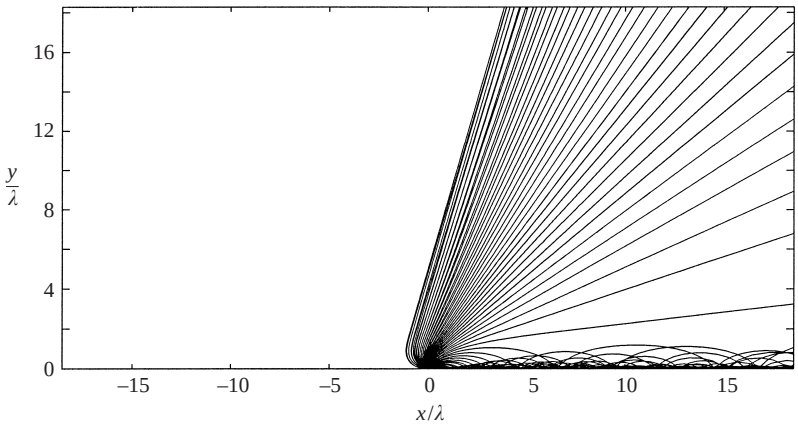

FIGURE 9. Ray trajectories at intermediate frequency, Case B. The procedure is the same as figure 6.

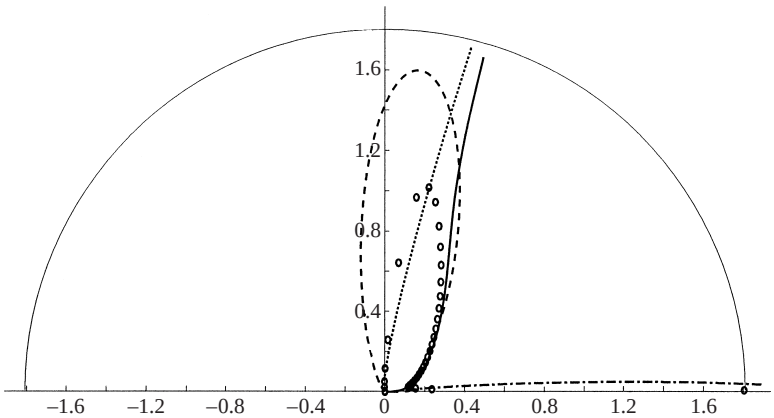

FIGURE 10. Pressure amplitude directivity at intermediate frequency, Case B. Pressure amplitude normalized by $\sqrt{Ro}$ (observer position $Ro \approx 15\lambda$) is shown in a polar plot. Notation is the same as figure 7. Pressure histories were recorded after time $t = 24$.

DNS in figure 10 is greater than the critical angle since the boundary layer has a finite thickness. Moreover, the peak amplitude is smaller than the theoretical prediction; nonetheless, the nature of the directivity pattern is close to the high-frequency limit. Note that the prediction of diffracted waves is based on a far-field asymptote which agrees better as the distance from the limiting ray becomes larger. Hence, the results for diffracted waves obtained from DNS do not follow the high-frequency limit near the critical angle.

Figures 11–13 show the high-frequency case (Case C). The computational domain is not large enough to evaluate the far-field asymptotes, but the radiation pattern of direct waves is very similar to the intermediate-frequency case (Case B). Since the boundary layer thickness is more appreciable, the structure of channelled waves becomes irregular compared with the previous cases (Cases A and B). Furthermore, diffracted waves become more noticeable as the frequency increases, and their radiation patterns clearly appear as general plane waves.

To observe the Mach number dependence, two additional Mach number cases ($M_\infty = 0.3$ in Case D and $M_\infty = 1.2$ in Case E at the intermediate frequency) were simulated. The results of Case D are presented in figures 14–16. As the free-stream Mach number decreases, the critical angle becomes higher and the peak amplitude decreases. The results for DNS and the high-frequency limit agree fairly well except very close to the critical angle. Near the critical angle, the directivity obtained from DNS does not form a sharp peak. This phenomenon commonly occurs in Cases B, C and E. The behaviour near the critical angle is discussed later.

In contrast, the results of the high Mach number case (Case E) are presented in figures 17–19. One can see that a large amount of acoustic energy is focused near the critical angle. Figure 19 shows that the low- and high-frequency limits nearly collapse to the critical angle and the peak becomes very sharp compared with the lower Mach number cases. Here, the limiting angle defined by the low-frequency limit is identical to the Mach angle ($\arcsin(1/M_\infty)$). As described in Appendix A, the critical angle of the high-frequency limit also asymptotically approaches the Mach angle as the Mach number increases.

In this study, since the size of the computational domain is limited, the peak angle of the DNS results and the asymptotic limits do not perfectly coincide. Although the distance of the observer positions relative to the acoustic wavelength was taken to be sufficiently large ($Ro \gg \lambda$), the effect of the boundary layer thickness was still large, particularly in Case C ($Ro = 7\delta_{BL}$). Therefore, the peak amplitude appears somewhat beyond the critical angle in DNS. Figure 20 depicts the directivity patterns at different distances of the observer positions. It demonstrates that the peak approaches the critical angle as the distance from the source becomes longer. If one could extend the computational domain, the DNS data should agree better with the high-frequency limit.

Another discrepancy in these comparisons is the behaviour near the critical angle. All polar plots commonly show that the sharp peak predicted by the high-frequency limit is considerably smeared and the peak amplitude tends to be smaller in the DNS. Recall that the wavenumber in the vertical direction can be expressed by $\bar{k}_y = \sqrt{\bar{n}^2(y) - \bar{k}_x^2}$, which approaches zero near the wall for the rays propagating close to the critical angle. Therefore, it is considered that the high-frequency limit fails in this region. As a result, the amplitude near the critical angle becomes smaller than the theoretical prediction. Note that the viscous effect hardly affects this roundness discrepancy: figure 21 shows that even if the Reynolds number is doubled, the directivity pattern remains very similar.

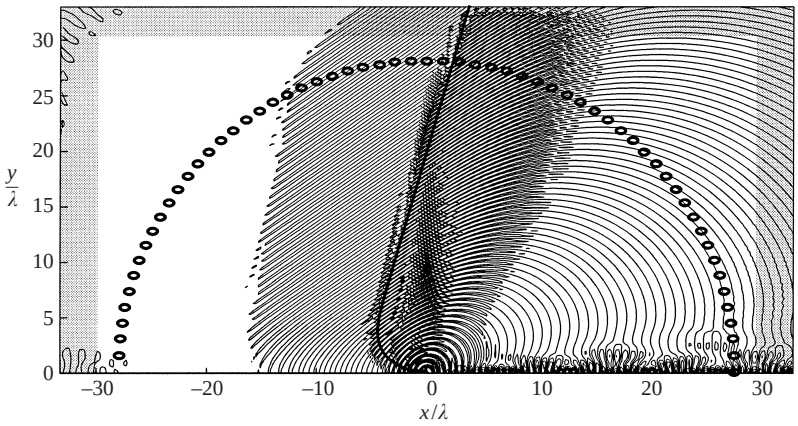

FIGURE 11. Pressure field at high-frequency, Case C ($M_\infty = 0.8$ and $\lambda/\delta_{BL} = 0.25$). Instantaneous pressure contours at time $t \approx 40$ are shown. Contour level and notation are the same as figure 5. The data were taken at $Ro \approx 28\lambda$ to evaluate the amplitude (figure 13).

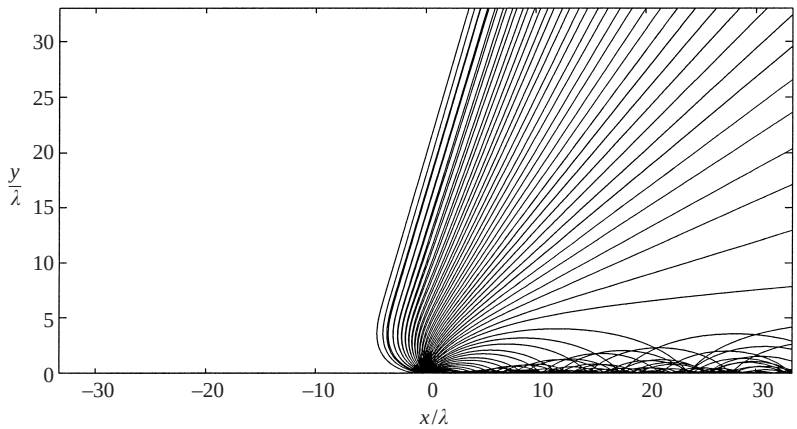

FIGURE 12. Ray trajectories at high-frequency, Case C. The procedure is the same as figure 6.

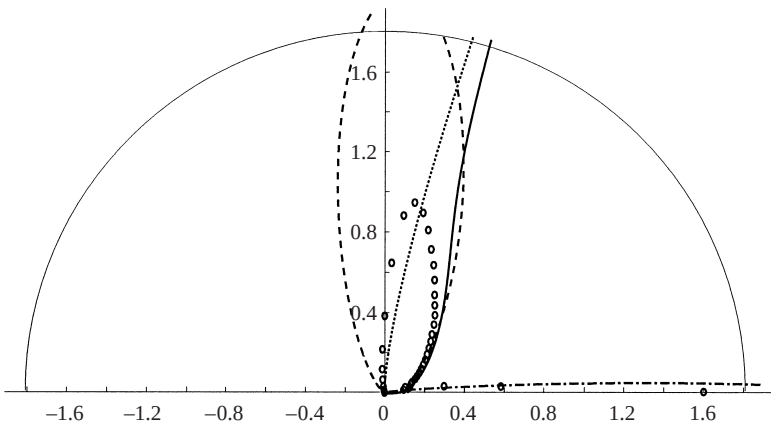

FIGURE 13. Pressure amplitude directivity at high-frequency, Case C. Pressure amplitude normalized by $\sqrt{Ro}$ (observer position $Ro \approx 28\lambda$) is shown in a polar plot. Notation is the same as figure 7. Pressure histories were recorded after time $t = 38$.

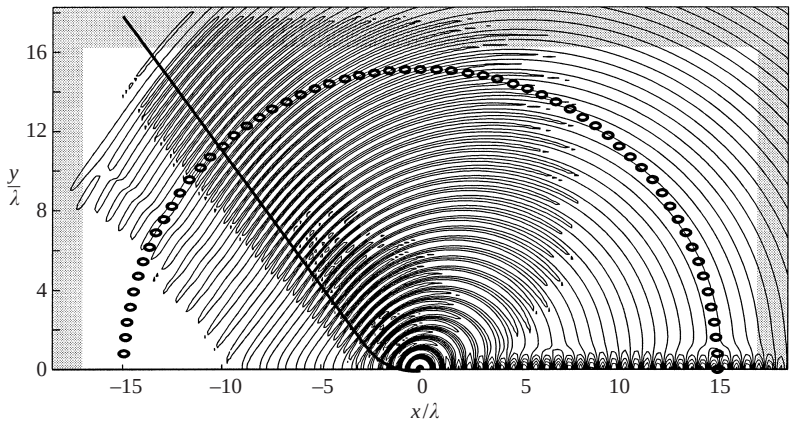

FIGURE 14. Pressure field at low Mach number, Case D ($M_\infty = 0.3$ and $\lambda/\delta_{BL} = 1.0$). Instantaneous pressure contours at time $t \approx 26$ are shown. Contour level and notation are the same as figure 5. The data were taken at $Ro \approx 15\lambda$ to evaluate the amplitude (figure 16).

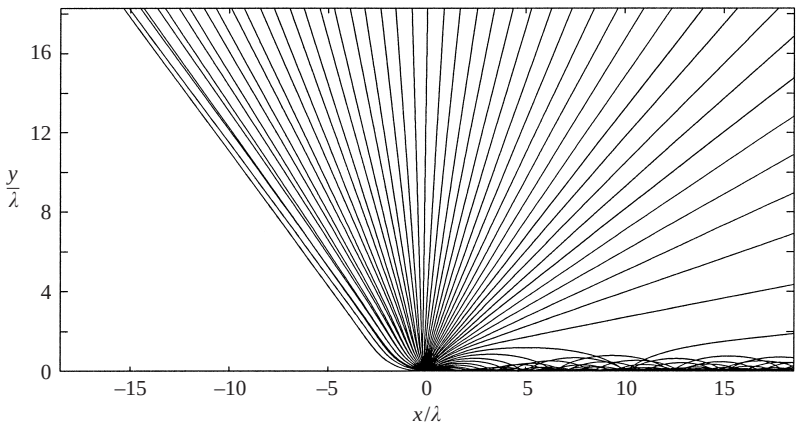

FIGURE 15. Ray trajectories at low Mach number, Case D. The procedure is the same as figure 6.

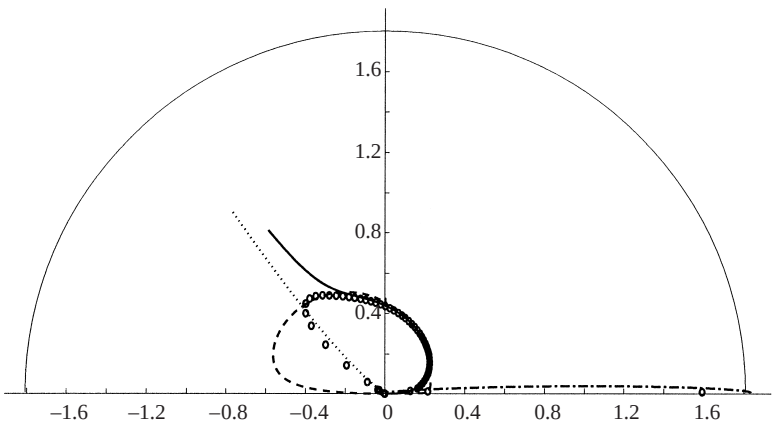

FIGURE 16. Pressure amplitude directivity at low Mach number, Case D. Pressure amplitude normalized by $\sqrt{Ro}$ (observer position $Ro \approx 15\lambda$) is shown in a polar plot. Notation is the same as figure 7. Pressure histories were recorded after time $t = 24$.

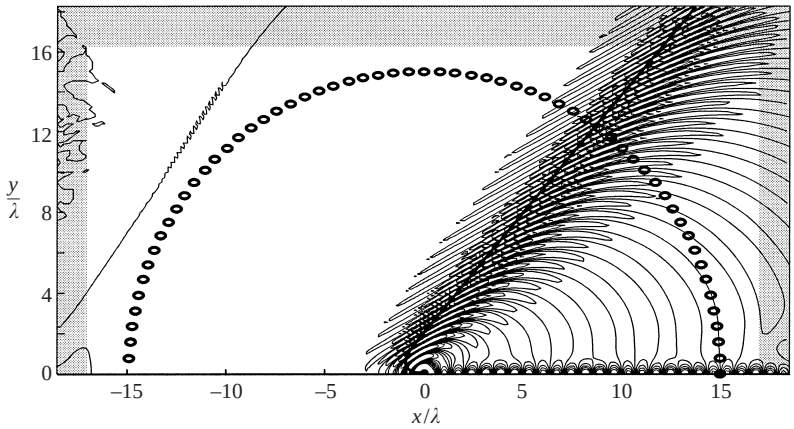

FIGURE 17. Pressure field at high Mach number, Case E ($M_\infty = 1.2$ and $\lambda/\delta_{BL} = 1.0$). Instantaneous pressure contours at time $t \approx 26$ are shown. Contour level and notation are the same as figure 5. The data were taken at $Ro \approx 15\lambda$ to evaluate the amplitude (figure 19).

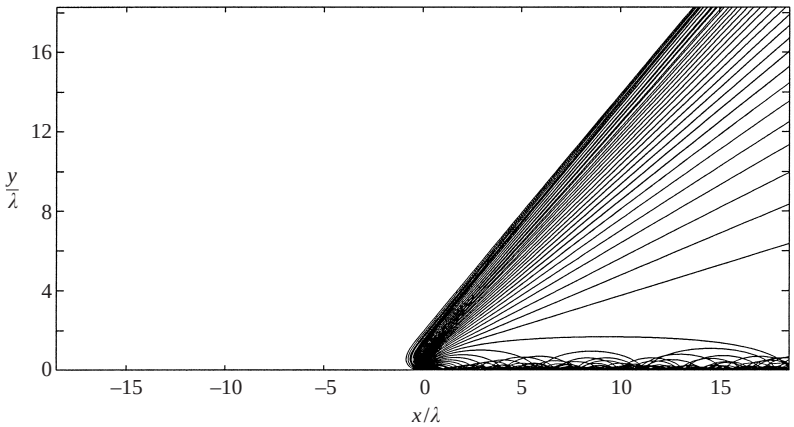

FIGURE 18. Ray trajectories at high Mach number, Case E. The procedure is the same as figure 6.

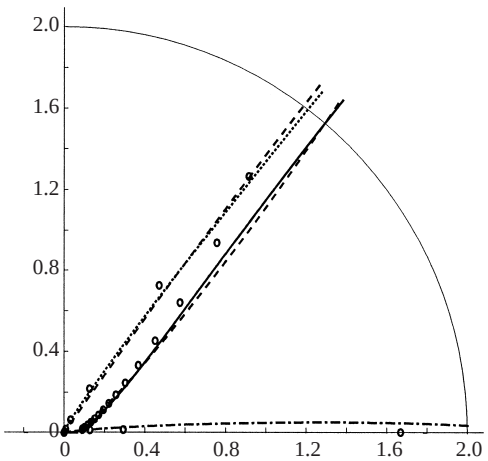

FIGURE 19. Pressure amplitude directivity at high Mach number, Case E. Pressure amplitude normalized by $\sqrt{Ro}$ (observer position $Ro \approx 15\lambda$) is shown in a polar plot. Notation is the same as figure 7. Pressure histories were recorded after time $t = 24$.

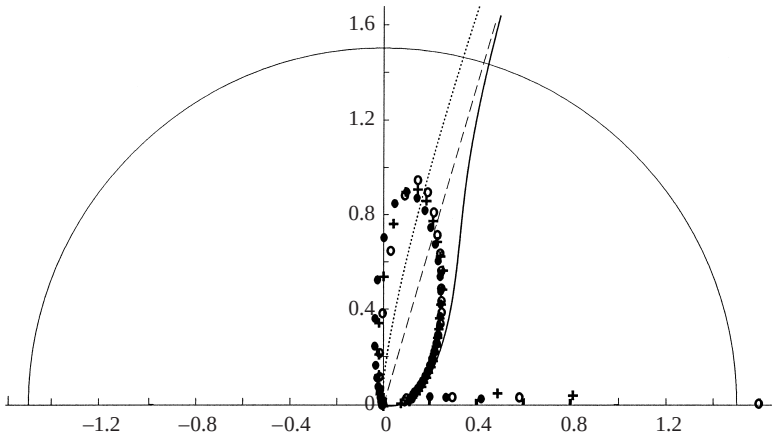

FIGURE 20. Directivity patterns at different observer distances in Case C. Flow conditions are the same as figure 13. Symbols are computed by DNS: ●, $Ro = 20\lambda$; +, $Ro = 24\lambda$; and ○, $Ro = 28\lambda$. — — — denotes the direction of the peak angle in the high-frequency limit. The rest of the notation is the same as figure 7.

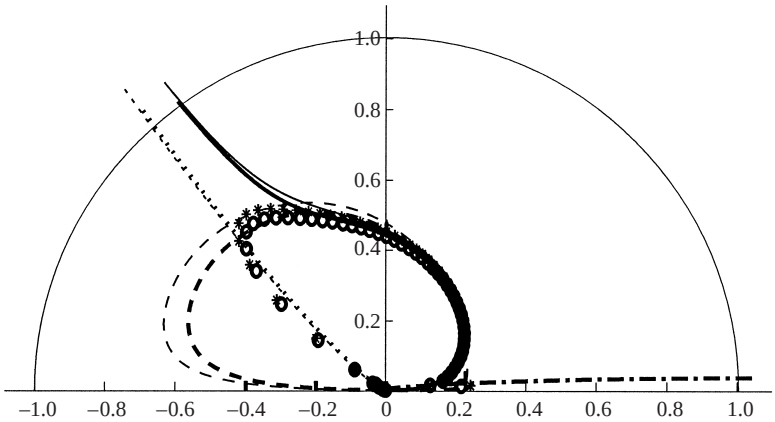

FIGURE 21. Directivity patterns at two different Reynolds numbers ($M_\infty = 0.3$). Flow conditions in one case (denoted by ○ for DNS and thicker lines for the asymptotes) are the same as figure 16 (Case D, $Re = 3750$). The other case (denoted by * for DNS and thiner lines for the asymptotes) is the same flow conditions except that the Reynolds number is doubled ($Re = 7500$). The rest of the notation is similar to figure 16.

4.2. *Channelled waves and diffracted waves*

Figures 22*a–e* compare the amplitude of channelled waves between the DNS and the theoretical predictions. As mentioned before, the numerical integration indicates that only one normal mode with a purely real k_{x_+} exists for each case under the flow conditions studied here. The results show that a single normal mode predicts the eigenmode shape and its amplitude fairly well. These shapes become thinner as the frequency increases. They also become thinner and their peaks become higher as the Mach number increases (although figures 22*b* and 22*e* depict very similar mode shapes).

As mentioned in Appendix E, direct waves penetrating the boundary layer cause interference with channelled waves, and this phenomenon makes it difficult to extract the eigenmode shape of channelled waves. In fact, due to the overestimate of the cross-

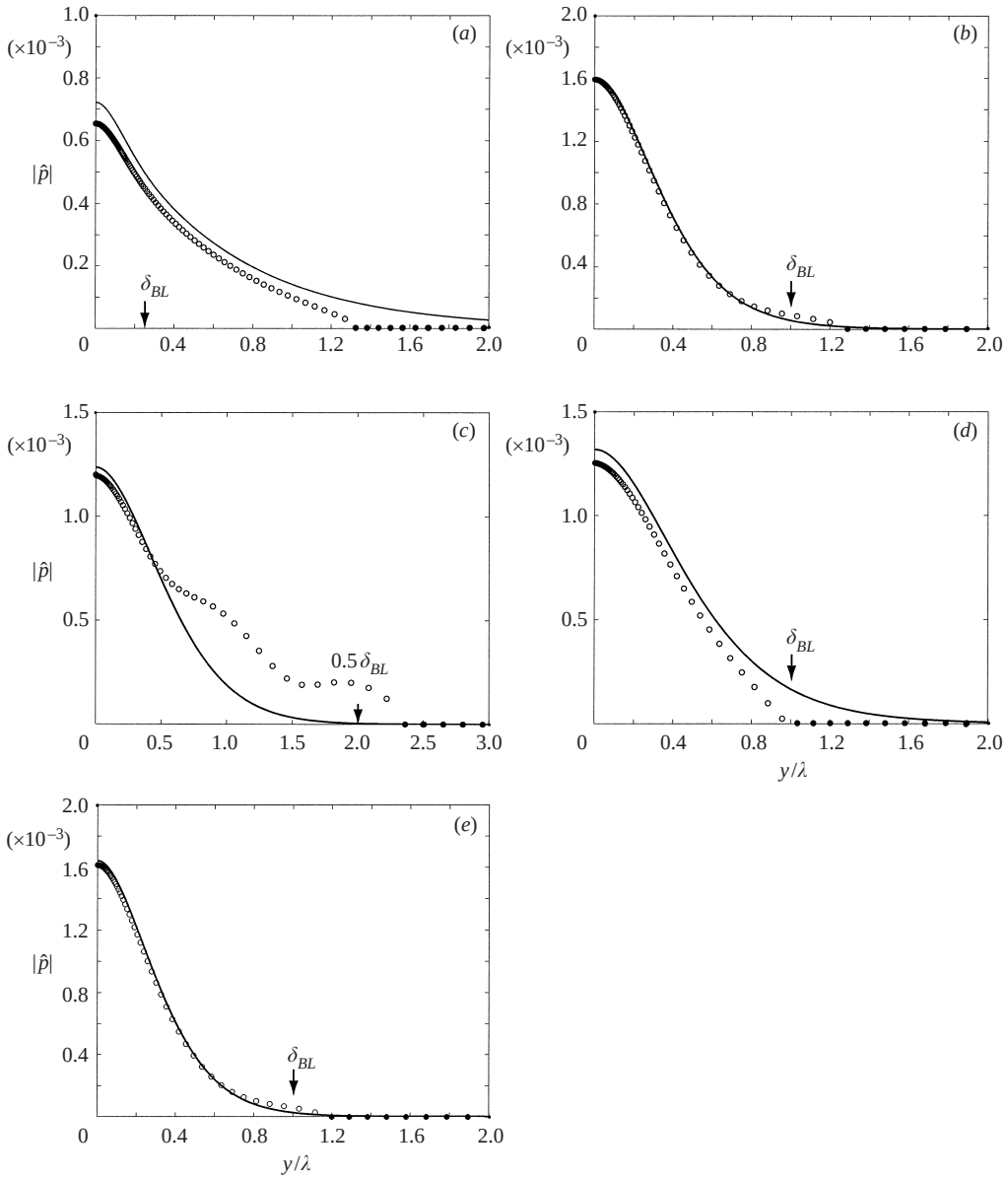

FIGURE 22. Pressure amplitude of channelled waves (a) at low-frequency, Case A ($M_\infty = 0.8$ and $\lambda/\delta_{BL} = 4.0$); ($b$) at intermediate frequency Case B ($M_\infty = 0.8$, $\lambda/\delta_{BL} = 1.0$; ($c$) at high frequency Case C ($M_\infty = 0.8$, $\lambda/\delta_{BL} = 0.25$); ($d$) at low Mach number, Case D ($M_\infty = 0.3$, $\lambda/\delta_{BL} = 1.0$); ($e$) at high Mach number, Case E ($M_\infty = 1.2$, $\lambda/\delta_{BL} = 1.0$) ——, Theoretical prediction; ○, DNS result; ●, the region in which the amplitude of channelled waves cannot be evaluated by DNS.

correlation terms in (E 8), the eigenmode shapes away from the wall become negative (denoted by •). Table 3 compares the wavenumbers of direct waves and channelled waves, showing that they are very similar at the low-frequency (Case A). Therefore, the interference pattern cannot be accurately captured in the computational domain, and the normal mode shape was calculated by simply taking an average in $x \in [3.6, 10.4]$. On the other hand, the intermediate-frequency cases give reasonable length periods

Case	$\bar{k}_{x_+}^{CH}$	$\bar{k}_{x_{\phi=0}}^{DR}$	Predicted period	Period from DNS
A	0.590	0.556	29.4	Not measurable
B	0.782	0.556	4.42	4.8
C	0.916	0.556	2.78	($\sim$ 4.0)
D	0.892	0.769	8.13	8.1
E	0.710	0.455	3.92	4.5

TABLE 3. Comparison of several properties for channelled waves. $\bar{k}_{x_+}^{CH}$ denotes the wavenumber of channelled waves computed using (E 1), and $\bar{k}_{x_{\phi=0}}^{DR}$ that of direct waves calculated setting $\phi = 0$ in (2.8). The fourth column 'Predicted period' denotes one length of period for the interference pattern given by $1/(\bar{k}_{x_+}^{CH} - \bar{k}_{x_{\phi=0}}^{DR})$, and the fifth column denotes that from the DNS data measuring from peak to peak.

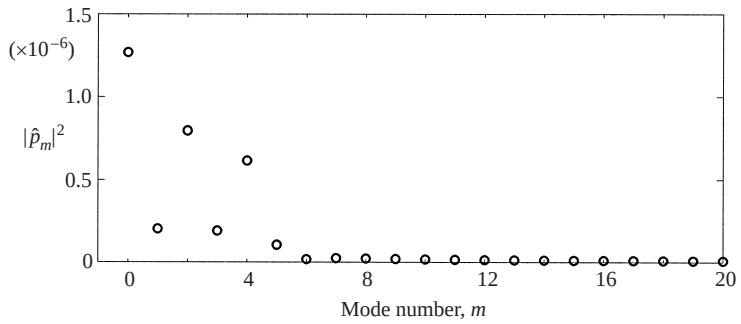

FIGURE 23. Fourier coefficients of the pressure amplitude square in the wavenumber domain in Case C. Absolute values of Fourier coefficients in the sampled interval (in the x-direction) are plotted. The zeroth mode corresponds to the constant (auto-correlations in (E 8)), and the second (lower mode) and the fourth (higher mode) modes indicate that there exist at least two interference patterns in this case.

(two periods were sampled for Cases B and E, and one for Case D); as a result, the theoretical predictions and the DNS results agree fairly well. At the high frequency (Case C), the amplitude in the wavenumber domain indicates that at least one more mode should exist (see figure 23). Referring to their wavenumbers in table 3, the lower peak (second component in figure 23) seems to be an uncaptured interference mode. Remember that only the mode with a purely real k_{x_+} is analysed in this study (although the authors could not find any other normal mode with a complex k_{x_+}), and the governing equation is assumed to be inviscid. It is conceivable that another normal mode that is slowly decaying, such as a viscous mode, is contaminated in the channelled waves; therefore, the theoretical prediction does not perfectly agree with DNS in the high-frequency case, as seen in figure 22*c*.

One can see that the interference patterns in the intermediate-frequency cases (Cases B, D and E) are generated by direct waves and channelled waves, but the length of periods do not exactly coincide with the theoretical predictions. If one calculates the periods of the interference patterns based on the waves-numbers of direct and channelled waves (see table 3), the theoretical predictions tend to be shorter than the DNS results. Since, within the boundary layer, direct waves are convected slower than in the free stream, their wavelength in the x-direction near the wall is compressed downstream. Remember that the wavenumbers of direct waves calculated

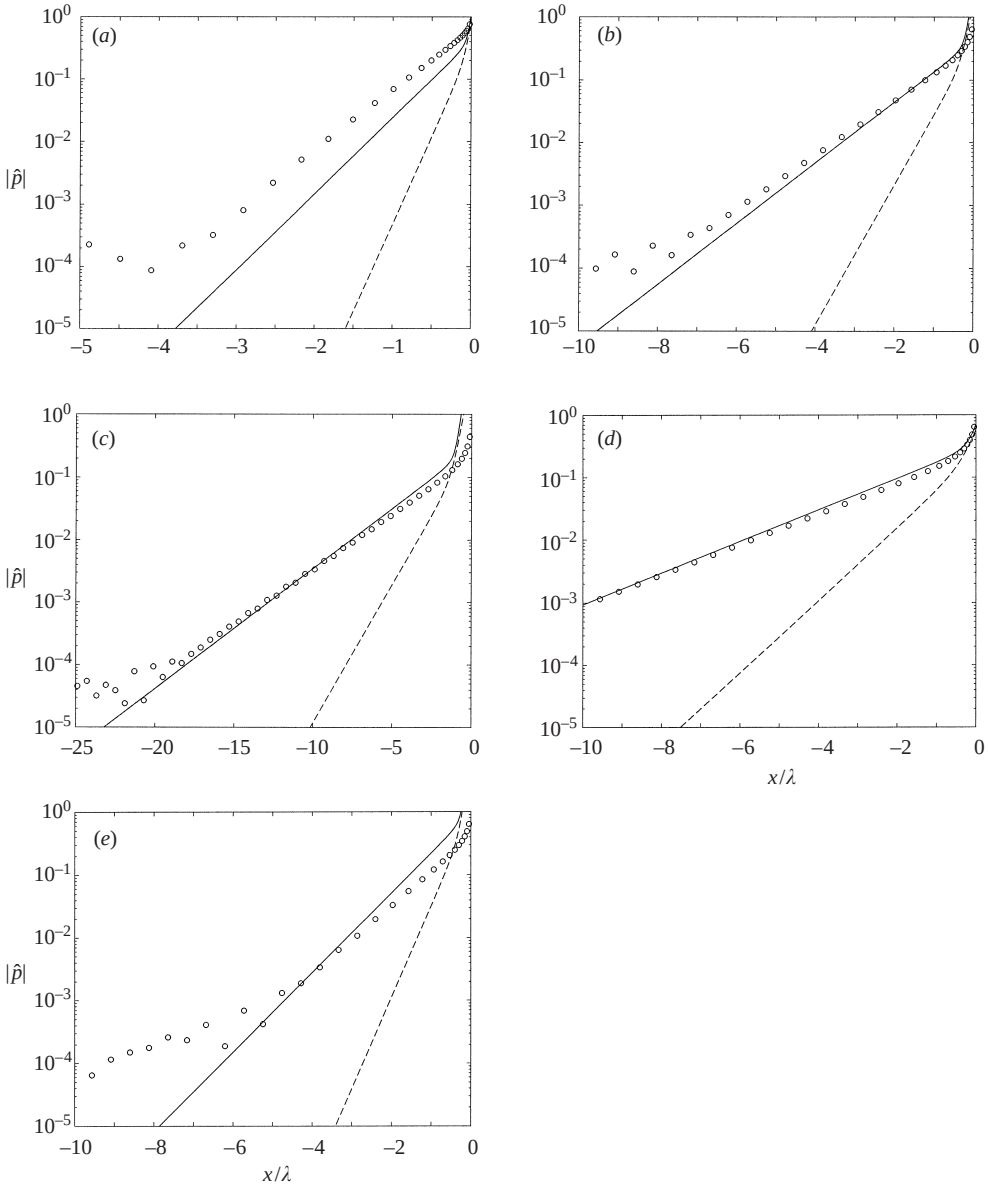

FIGURE 24. Pressure amplitude of diffracted waves at low-frequency, Case A ($M_\infty = 0.8$ and $\lambda/\delta_{BL} = 4.0$); (*b*) intermediate frequency, Case B ($M_\infty = 0.8$, $\lambda/\delta_{BL} = 1.0$); (*c*) high frequency, Case C ($M_\infty = 0.8$, $\lambda/\delta_{BL} = 0.25$); (*d*) low Mach number, Case D ($M_\infty = 0.3$, $\lambda/\delta_{BL} = 1.0$); (*e*) high Mach number, Case E ($M_\infty = 1.2$, $\lambda/\delta_{BL} = 1.0$). Asymptotic formulas: ——, $\mathscr{Z}^\bullet = 0$; — — —, $\mathscr{Z}^\bullet \to \infty$; ○, DNS result.

in table 3 assume the boundary layer thickness to be infinitely thin. Thus, the periods of the interference patterns tend to be longer in the DNS.

Figure 24 compares the pressure amplitude of diffracted waves between the DNS results and the theoretical predictions. Figure 24(*a*) depicts that at the low frequency (Case A), the DNS result becomes considerably larger than the analytical predictions based on both Neumann ($\mathscr{Z} = 0$) and Dirichlet ($|\mathscr{Z}| \to \infty$) boundary conditions. But, as figures 24 *b*, *c* (Cases B and C) show, when the frequency increases (with a

Case	Asymptotic formula	Numerical integration
A	$-1.258 - \mathrm{i}\,0.447$	$-1.282 - \mathrm{i}\,0.347$
B	$-1.102 - \mathrm{i}\,0.177$	$-1.109 - \mathrm{i}\,0.161$
C	$-1.041 - \mathrm{i}\,0.070$	$-1.042 - \mathrm{i}\,0.068$
D	$-1.053 - \mathrm{i}\,0.092$	Does not converge
E	$-1.134 - \mathrm{i}\,0.232$	$-1.145 - \mathrm{i}\,0.204$

TABLE 4. Comparison of the wavenumber $\bar{k}_x$ between the asymptotic formula (2.41) and the numerical integration (E 1).

fixed Mach number), the DNS results agree fairly well with the predictions based on the Neumann boundary condition. Since the acoustic impedance becomes finite on a viscous wall as discussed in § 2.5, the decay rates of DNS are expected to be somewhere in between these two asymptotes. However, the actual results are even slightly slower than the prediction based on the Neumann boundary condition. Therefore, it is deduced that at low frequencies, the decay rate is slower than that predicted by the high-frequency asymptotic formula (2.41). Accordingly, this frequency dependence totally overcomes the effect of non-zero acoustic impedance.

This point is clarified by comparing the complex $\bar{k}_{x_-}$ obtained from the high-frequency asymptote (2.41) and from the numerical integration (E 1) (see Appendix E). These values are shown in table 4. Based on the asymptotic formula, the complex wavenumbers $\bar{k}_x$ are predicted quite well; however, in Case A the decay rate ($-\mathrm{Im}[\bar{k}_x]$) is over-predicted compared with the numerical integration. Therefore, it is fair to conclude that the actual decay rate of the diffracted waves tends to become slower than the high-frequency asymptote as the frequency decreases.

In terms of the Mach number dependence, the series of figures 24 *b*, *d*, *e* shows that as the Mach number increases, the decay rate of diffracted waves becomes greater. In the supersonic case (figure 24*e*), the DNS result deviates considerably from the theoretical prediction although there is no difference in the theoretical formula compared to the subsonic case: the amplitude part becomes far smaller, and the decay rate becomes slightly slower. In fact, table 4 demonstrates that the high-frequency asymptotic formula over-estimates the decay rate in Case E. It should be emphasized that when (2.41) is derived, the interval of the integration $y \in [y^*, 0]$ is assumed much longer than the acoustic wavelength and $\bar{n}^2 - \bar{k}_x^2$ to be small due to the high-frequency limit, and the parabolic fitting is used. However, as $\bar{n}^2 - \bar{k}_x^2$ increases, its variation during the interval needs to be precisely calculated. Note that knowing $\bar{n}_0 = 1$, the deviation from $\bar{k}_x = -1$ indicates the magnitude of the second term in (2.41). Thus, the asymptotic expressions for Case E as well as Case A provide worse estimates of the decay rate.

Finally, to provide an overview of the modes of channelled and diffracted waves, the normalized wavenumbers, $\bar{k}_x$, are plotted in the complex plane. Figures 25 and 26 represent the frequency and Mach number dependence of the wavenumber, respectively. These values were computed based on numerical integration (E 1), and the values at the high-frequency limit for diffracted waves (2.41) are also shown for reference. Figure 25 indicates that as the frequency becomes higher, the wavenumber of channelled waves approaches $\bar{k}_x = 1$, while that of diffracted waves approaches $\bar{k}_x = -1$, decreasing its imaginary part. Likewise, figure 26 indicates that as the Mach number decreases, a very similar tendency appears. As expected, as the frequency increases or the Mach number decreases, the effect of the mean flow asymptotically becomes

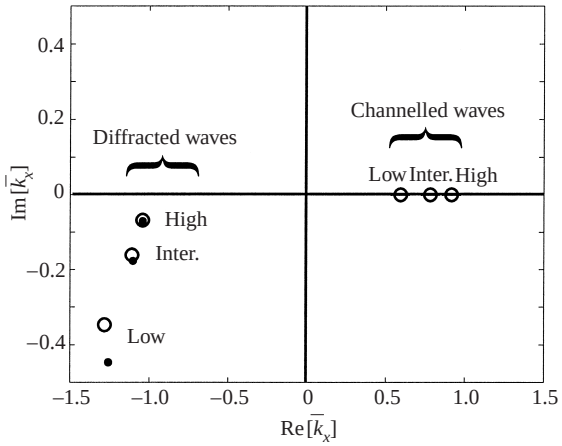

FIGURE 25. Frequency dependence of the wavenumber. Complex wavenumbers $\bar{k}_x$ of channelled waves and the first mode of diffracted waves are plotted. ○, computed based on numerical integration (E 1), and ●, calculated using the high-frequency asymptotic formula (2.41).

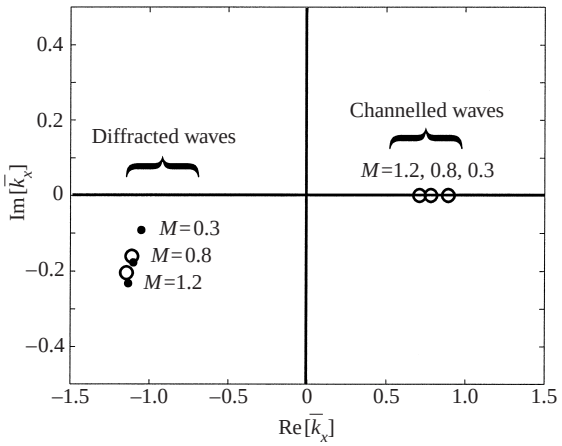

FIGURE 26. Mach number dependence of the wavenumber. Notation is the same as figure 25. The wavenumber of diffracted waves for $M = 0.3$ could not be computed based on numerical integration.

negligible. Furthermore, it is consistently illustrated that the analytical predictions of diffracted waves deteriorate as the imaginary part of $\bar{k}_x$ increases.

Note that although these comparisons show fairly reasonable results, the accuracy of the acoustic impedance in the DNS is uncertain. From table 2, the number of the grid points within the length scale of the vorticity (or entropy) mode is about 3–6 (see figure 27, for example), which is not sufficient to resolve these disturbance scales. To accurately assess the acoustic impedance model, finer mesh spacing may be necessary, which is able to resolve the mode coupling on a viscous wall as described in § 2.5.

5. Conclusions

Regarding direct waves, the high-frequency asymptotic Green's function approximates the DNS results best except for the low-frequency case ($\lambda/\delta_{BL} = 4.0$ and $M_\infty = 0.8$). At a low frequency the amplitude peak appears somewhat beyond the

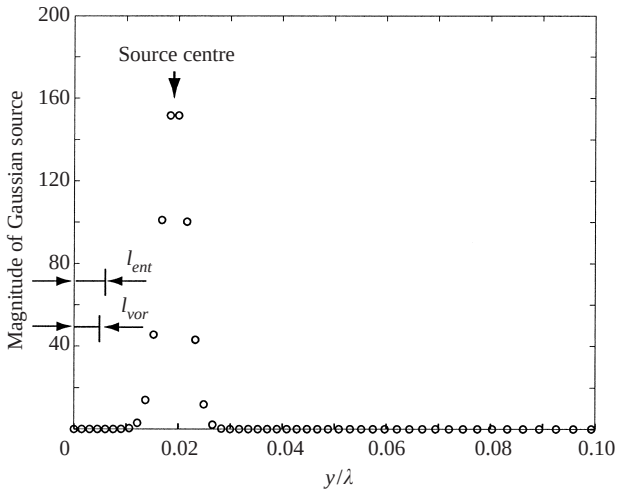

FIGURE 27. Comparison of the length scales in Case B. The length scales of the vorticity and entropy modes are illustrated. The Gaussian source distribution for DNS ($\exp(-(x_2 - x_{2p})^2/2\sigma_2^2/\sqrt{2\pi\sigma_2^2})$) in the vertical direction is plotted at every grid point.

critical angle. To simulate the radiation pattern of the low-frequency limit in DNS, the forcing frequency needs to be further decreased.

To analyse channelled waves, an adjoint operator of the transformed third-order convective wave equation is introduced by imposing the mixed-type boundary condition, and the corresponding inner product is defined. Based on the normal mode decomposition, the shapes and magnitudes of the eigenmodes in DNS are successfully predicted. Note that this method is potentially applicable to various types of acoustic problems in two-dimensional transversely sheared flows.

In the shadow zone, diffracted waves are formulated in the high-frequency limit, and the comparison with DNS agrees fairly well based on the Neumann boundary condition. The results also show that as the frequency decreases or the Mach number increases, the actual decay rate of diffracted waves becomes slower than the high-frequency limit.

Thus, the expressions for Green's functions in a boundary layer are well established, and they should improve the physical understanding of sound radiation from noise sources near the wall. The extension of these formulas to multipoles and moving sources for practical use is relatively straightforward (refer to Suzuki 2001). In terms of far-field noise radiation, the high-frequency limit of direct waves should be able to predict the directivity fairly well. However, the comparison with the DNS results implies that the amplitude may be over-estimated, especially near the peak angle. Therefore, more detailed analysis near the critical angle may be required for accurate prediction. Regarding the interior noise, the DNS results indicate that channelled waves should be dominant inside the boundary layer, particularly at high-frequencies; moreover, their decay rate is slower than that of direct waves. This implies that the pressure fluctuation on the wall is strongly influenced by the upstream disturbances. Thus, one may need to include a large domain in the upstream direction to predict the interior noise due to turbulence near the wall.

It should be mentioned that these analyses are based on laminar boundary layer profiles. However, the asymptotic formulas (low- and high-frequency direct waves and high-frequency diffracted waves) are independent of the mean velocity profile. There-

fore, these formulas are expected to be valid even for turbulent velocity profiles as long as the turbulent length scale is reasonably smaller than the acoustic wavelength. (Note that since the boundary layer thickness in this study is defined based on the velocity gradient on the wall, it becomes thinner as the velocity gradient on the wall becomes steeper.) Of course, when the acoustic wavelength becomes comparable with the turbulent length scale, such as the eddy scale, significant sound scattering should occur and the theoretical prediction would be no longer valid. Regarding channelled waves, the eigenmode shape becomes broader as the frequency decreases; therefore, it is similarly expected that the mean velocity profile of turbulent flows should give a reasonable estimate for channelled waves at low-frequencies. Likewise, the effects of the spreading rate of the boundary layer also need to be investigated for practical use.

The authors would like to thank Professor Joseph B. Keller for many useful suggestions. We gratefully acknowledge the financial support by NASA Ames Research Center (grant number NCC-255 and NAG 2-1373).

Appendix A. Critical angle

As described in § 2.2, direct waves cannot propagate beyond the critical angle in the high-frequency limit. In the expressions for the high-frequency Green's functions (2.14) or (2.15), one of the terms in the denominator, $((\bar{n}_\eta^\star)^2 - (\bar{k}_x^\star)^2)^{1/4}$ or $((\bar{n}_\eta^\star)^2 - (\bar{k}_x^\star)^2 - (\bar{k}_z^\star)^2)^{1/4}$, can vanish. When the source is located very close to the wall, one can assume $\bar{n}_\eta = 1$. Hence, the denominator vanishes when

$$\bar{k}_x = \frac{1}{1 - M_\infty^2}\left(-M_\infty + \frac{\cos\phi}{\sqrt{1 - M_\infty^2 \sin^2\phi}}\right) \approx 1. \tag{A 1}$$

This gives

$$\phi_{cr} = \begin{cases} \pi - \arcsin\left[\sqrt{\dfrac{1 - (M_\infty^2 + M_\infty - 1)^2}{1 - M_\infty^2(M_\infty^2 + M_\infty - 1)^2}}\right], & 0 \leqslant M < M_{90}^{high} \\ \arcsin\left[\sqrt{\dfrac{1 - (M_\infty^2 + M_\infty - 1)^2}{1 - M_\infty^2(M_\infty^2 + M_\infty - 1)^2}}\right], & M_{90}^{high} \leqslant M. \end{cases} \tag{A 2}$$

Here, $M_{90}^{high} = (\sqrt{5} - 1)/2 \approx 0.618$. Note when $M_\infty \to \infty$, the critical angle asymptotically reaches

$$\lim_{M_\infty \to \infty} \phi_{cr} = \arcsin\left(\frac{1}{M_\infty}\right), \tag{A 3}$$

which is identical to the Mach angle. Equation (A 2) was used to draw the lines for the critical angles in the figures showing instantaneous pressure contours.

Appendix B. Normal mode decomposition for the temporal problem

As discussed in § 2.3 for channelled waves, the conservation form (2.26) includes an inconvenient boundary term for a temporal problem. In general, one substitutes

arbitrary disturbances into Π_m and a certain known normal mode into $\Pi_n^\dagger$, so that the nth mode can be extracted. However, the boundary term

$$\left(\frac{\partial \Pi_m}{\partial t}\frac{\partial \Pi_n^\dagger}{\partial t} - 3\frac{\mathrm{d}M}{\mathrm{d}y}\frac{\partial \Pi_n^\dagger}{\partial x}\right)_{y=0}$$

remains if one tries to solve a temporal problem using (2.26). To produce a suitable boundary term, modify the 'inner product' by adding a boundary term to it. Thus, (2.26) can be rewritten as follows:

$$\int_0^\infty \Pi_n^\dagger[\mathscr{L}(\omega_m, k_{xm})\Pi_m]\,\mathrm{d}y + \int_0^\infty \Pi_m[\mathscr{L}^\dagger(\omega_n, k_{xn})\Pi_n^\dagger]\,\mathrm{d}y - \Pi_m\left(\frac{\partial^2 \Pi_n^\dagger}{\partial t \partial y} + 3\frac{\mathrm{d}M}{\mathrm{d}y}\frac{\partial \Pi_n^\dagger}{\partial x}\right)_{y=0}$$
$$= \frac{\partial}{\partial t}\left[\int_0^\infty J_t(\Pi_n^\dagger, \Pi_m)\,\mathrm{d}y - \left(\Pi_m \frac{\partial \Pi_n^\dagger}{\partial y}\right)_{y=0}\right] + \frac{\partial}{\partial x}\int_0^\infty J_x(\Pi_n^\dagger, \Pi_m)\,\mathrm{d}y, \tag{B 1}$$

where Π_m, $\Pi_n^\dagger$, $\mathscr{L}$, $\mathscr{L}^\dagger$, J_t, and J_x are as defined in § 2.3. As seen in (B 1), the boundary condition for $\Pi_n^\dagger$ is still the same as (2.25),

$$\frac{\partial \Pi_n^\dagger}{\partial y} = 3\frac{k_x}{\omega_n}\frac{\mathrm{d}M}{\mathrm{d}y}\Pi_n^\dagger.$$

Thus, in the temporal problem only the first term on the right-hand side remains,

$$\mathrm{i}(\omega_n - \omega_m)\left[\int_0^\infty J_t(\Pi_n^\dagger, \Pi_m)\,\mathrm{d}y - \left(\Pi_m \frac{\partial \Pi_n^\dagger}{\partial y}\right)_{y=0}\right] = 0, \tag{B 2}$$

and the problem can be solved using the same method as described in § 2.3.

Appendix C. Derivation of the viscous boundary conditions with a high free-stream Mach number

To derive appropriate viscous boundary conditions with a high free-stream Mach number, first the derivation of the viscous boundary conditions with no mean flow is revisited (refer to Pierce 1989); subsequently, these boundary conditions are extended to a highly sheared mean flow using an asymptotic analysis. Recall that it is assumed that $Re_{ac}^{-1/2} \ll \min\{|\lambda/\delta_{BL}|, |\delta_{BL}/\lambda|\}$ in this derivation.

To find the solution for each disturbance mode, follow the derivation of the so-called 'Kirchhoff's dispersion relation' (Kirchhoff 1868) retaining the mean velocity in the x-direction (denoted by U_x). Accordingly, the linearized Navier–Stokes equations can be rewritten as

$$\frac{\mathrm{D}\hat{\rho}}{\mathrm{D}t} + \rho(\nabla \cdot \hat{\boldsymbol{u}}) = 0, \tag{C 1}$$

$$\rho\left(\frac{\mathrm{D}\hat{u}_x}{\mathrm{D}t} + \hat{u}_y\frac{\partial U_x}{\partial y}\right) + \frac{\partial \hat{p}}{\partial x} = \mu\left[\Delta\hat{u}_x + \frac{1}{3}\frac{\partial}{\partial x}(\nabla \cdot \hat{\boldsymbol{u}})\right], \tag{C 2}$$

$$\rho\frac{\mathrm{D}\hat{u}_y}{\mathrm{D}t} + \frac{\partial \hat{p}}{\partial y} = \mu\left[\Delta\hat{u}_y + \frac{1}{3}\frac{\partial}{\partial y}(\nabla \cdot \hat{\boldsymbol{u}})\right], \tag{C 3}$$

$$\frac{\mathrm{D}\hat{s}}{\mathrm{D}t} = 2\frac{\mu}{\rho T}\frac{\partial U_x}{\partial y}\left(\frac{\partial \hat{u}_x}{\partial y} + \frac{\partial \hat{u}_y}{\partial x}\right) + \frac{\kappa}{\rho C_p}\Delta\left(\hat{s} + \frac{\hat{p}}{\rho T}\right), \tag{C 4}$$

where $\mathrm{D}/\mathrm{D}t \equiv \partial/\partial t + U_x \partial/\partial x$, and quantities with a hat represent small disturbances. Here, the ideal gas law is used, and the mean velocity is assumed to be parallel and purely transversely sheared. But the rest of the mean quantities, such as p, ρ, T, μ, etc., are assumed constant everywhere. Furthermore, assume that each quantity can be expressed in the form $\sim f(y)\, e^{-\mathrm{i}(\omega t - k_x x)}$. After some algebra, (C 1)–(C 4) can be rewritten as the following equation system:

$$-\frac{a^2}{\Omega^2}\Delta\hat{s} + \mathrm{i}\frac{C_p}{\Omega}\left[1 - \mathrm{i}\frac{4}{3}\frac{\mu}{\rho\Omega}\Delta\right](\boldsymbol{\nabla}\cdot\hat{\boldsymbol{u}}) - \frac{a^2}{\Omega^2}\Delta\left[-\mathrm{i}\frac{C_p}{\Omega}(\boldsymbol{\nabla}\cdot\hat{\boldsymbol{u}})\right] - \mathrm{i}\frac{2k_x C_p}{\Omega^2}\frac{\partial U_x}{\partial y}\hat{u}_y = 0, \quad \text{(C 5)}$$

$$\frac{\partial}{\partial y}\hat{s} + \frac{\partial}{\partial y}\left[-\mathrm{i}\frac{C_p}{\Omega}(\boldsymbol{\nabla}\cdot\hat{\boldsymbol{u}})\right] - \frac{1}{3}\frac{\mu C_p}{\rho a^2}\frac{\partial}{\partial y}(\boldsymbol{\nabla}\cdot\hat{\boldsymbol{u}}) - \mathrm{i}\frac{\Omega C_p}{a^2}\left[1 - \mathrm{i}\frac{\mu}{\rho\Omega}\Delta\right]\hat{u}_y = 0, \quad \text{(C 6)}$$

$$\left[1 - \mathrm{i}\frac{\gamma\kappa}{\rho C_p \Omega}\Delta\right]\hat{s} - \mathrm{i}\frac{(\gamma-1)\kappa}{\rho\Omega C_p}\Delta\left[-\mathrm{i}\frac{C_p}{\Omega}(\boldsymbol{\nabla}\cdot\hat{\boldsymbol{u}})\right] - 2\frac{\mu}{k_x\rho\Omega T}\frac{\partial U_x}{\partial y}\left[\frac{\partial}{\partial y}(\boldsymbol{\nabla}\cdot\hat{\boldsymbol{u}}) - \Delta\hat{u}_y - 2k_x^2\hat{u}_y\right] = 0, \quad \text{(C 7)}$$

where $\Omega \equiv \omega - k_x U_x$.

To estimate the order of each term, first consider a quiescent flow; namely $U_x \equiv 0$. In this case, simply follow Pierce (1989): $\mathrm{d}U_x/\mathrm{d}y = 0$ and Ω is replaced by ω. Accordingly, $\partial/\partial y$ can be simply replaced by $\mathrm{i}k_y$. By defining $\epsilon_\mu \equiv \mathrm{i}\mu\omega/\rho a^2$, $\epsilon_\kappa \equiv \mathrm{i}\kappa\omega/\rho a^2 C_p$, $\boldsymbol{X} \equiv a^2|\boldsymbol{k}|^2/\omega^2$, $\boldsymbol{Y} \equiv \mathrm{i}ak_y/\omega$, $\hat{d} \equiv -\mathrm{i}C_p/\omega(\boldsymbol{\nabla}\cdot\hat{\boldsymbol{u}})$, and $\hat{v}_y \equiv -\mathrm{i}C_p/a\hat{u}_y$, system (C 5)–(C 7) in a quiescent flow can be expressed as

$$(1 + \gamma\epsilon_\kappa \boldsymbol{X})\hat{s} + (\gamma - 1)\epsilon_\kappa \boldsymbol{X}\hat{d} = 0, \quad \text{(C 8)}$$

$$\boldsymbol{X}\hat{s} - (1 - \boldsymbol{X} + \tfrac{4}{3}\epsilon_\mu \boldsymbol{X})\hat{d} = 0, \quad \text{(C 9)}$$

$$\boldsymbol{Y}\hat{s} + (1 - \tfrac{1}{3}\epsilon_\mu)\boldsymbol{Y}\hat{d} + (1 + \epsilon_\mu \boldsymbol{X})\hat{v}_y = 0. \quad \text{(C 10)}$$

When this simultaneous equation system has a non-trivial solution, its determinant must be zero; namely

$$(1 + \epsilon_\mu \boldsymbol{X})[\epsilon_\kappa(\tfrac{4}{3}\gamma\epsilon_\mu - 1)\boldsymbol{X}^2 - (1 - \tfrac{4}{3}\epsilon_\mu - \gamma\epsilon_\kappa)\boldsymbol{X} + 1] = 0. \quad \text{(C 11)}$$

This is called 'Kirchhoff's dispersion relation' (Kirchhoff 1868). One obvious solution to (C 11) is $\boldsymbol{X} = -1/\epsilon_\mu$, which is referred to as the 'vorticity mode'. The other two solutions can be approximately computed assuming $|\epsilon_\mu|$, $|\epsilon_\kappa| \ll 1$ (the orders of ϵ_μ and ϵ_κ are the same, denoted by ϵ in this section, which is different from the one defined in § 2.1): $\boldsymbol{X} \approx -1/\epsilon_\kappa$, which is called the 'entropy mode'; and $\boldsymbol{X} \approx 1$, the 'acoustic mode'. Notice that two dispersion relations, for the vorticity and entropy modes, are the same order ($\boldsymbol{X} = O(\epsilon^{-1})$), and that of the acoustic mode is $\boldsymbol{X} = O(1)$.

Next, extend this previous theory to a shear flow. Notice that $\partial/\partial y$ and Ω do not commute in such a case. To rewrite the equation system (C 5)–(C 7), the following relations are useful:

$$-\mathrm{i}\frac{C_p}{\Omega}\boldsymbol{Y}(\boldsymbol{\nabla}\cdot\hat{\boldsymbol{u}}) = (\boldsymbol{Y} - \Gamma)\hat{d}, \quad \text{(C 12)}$$

$$-\mathrm{i}\frac{C_p}{\Omega}\boldsymbol{X}(\boldsymbol{\nabla}\cdot\hat{\boldsymbol{u}}) = (\boldsymbol{X} + 2\Gamma\boldsymbol{Y} + \Sigma)\hat{d}, \quad \text{(C 13)}$$

where

$$\boldsymbol{X} \equiv -\frac{a^2}{\Omega^2}\Delta, \quad \boldsymbol{Y} \equiv \frac{a}{\Omega}\frac{\partial}{\partial y}, \quad \Gamma \equiv -\frac{a}{\Omega^2}\frac{\partial \Omega}{\partial y}, \quad \Sigma \equiv -\frac{a^2}{\Omega^3}\frac{\partial^2 \Omega}{\partial y^2}, \quad \hat{d} \equiv -\mathrm{i}\frac{C_p}{\Omega}(\nabla \cdot \hat{\boldsymbol{u}}).$$

Note that the operators $\boldsymbol{X}$ and $\boldsymbol{Y}$ are not independent of each other. Thus, the equation system in a shear flow can be written as

$$(1+\gamma\epsilon_\kappa \boldsymbol{X})\hat{s} + [(\gamma-1)\epsilon_\kappa \boldsymbol{X} + 2\epsilon_\mu \Gamma \chi^{-1}(\boldsymbol{Y}+\Gamma)]\hat{d} + 2\epsilon_\mu \Gamma \chi^{-1}(\boldsymbol{X}-2\chi)\hat{v}_y = 0, \quad \text{(C 14)}$$

$$\boldsymbol{X}\hat{s} - (1-\boldsymbol{X}+\tfrac{4}{3}\epsilon_\mu \boldsymbol{X} + \tfrac{8}{3}\epsilon_\mu \Gamma \boldsymbol{Y} + \tfrac{4}{3}\epsilon_\mu \Sigma)\hat{d} + 2\Gamma \hat{v}_y = 0, \quad \text{(C 15)}$$

$$\boldsymbol{Y}\hat{s} + (\boldsymbol{Y} - \tfrac{1}{3}\epsilon_\mu \boldsymbol{Y} + \tfrac{1}{3}\epsilon_\mu \Gamma)\hat{d} + (1+\epsilon_\mu \boldsymbol{X})\hat{v}_y = 0, \quad \text{(C 16)}$$

where $\chi \equiv a^2 k_x^2/\Omega^2$ and $\hat{v}_y \equiv -\mathrm{i}(C_p/a)\hat{u}_y$. Here, consider the dimension of each term.

$$\Gamma \sim \left|\frac{M_\infty a^2}{\omega^2 \lambda \delta_{BL}}\right| \sim \frac{M_\infty \lambda}{\delta_{BL}},$$

which is common in all modes. In this analysis, assume both $M = O(1)$ and $\lambda/\delta_{BL} = O(1)$; accordingly, $\Gamma = O(1)$. Likewise, $\chi = O(1)$ and $\Sigma = O(1)$. In the acoustic mode, since $\boldsymbol{X} = O(1)$, then $\boldsymbol{Y} = O(1)$ from the previous analysis; hence, one should expand each term in terms of ϵ to asymptotically solve this equation system. However, in the vorticity or entropy mode, $\boldsymbol{X} = O(\epsilon^{-1})$ leads $\boldsymbol{Y} = O(\epsilon^{-1/2})$. Therefore, one should expand each term in terms of $\epsilon^{1/2}$ in these modes.

First, to solve the acoustic mode, expand each term as follows:

$$\hat{s} \approx \hat{s}_0 + \epsilon\hat{s}_1 + \epsilon^2\hat{s}_2 + \cdots, \quad \hat{d} \approx \hat{d}_0 + \epsilon\hat{d}_1 + \epsilon^2\hat{d}_2 + \cdots, \quad \hat{v}_y \approx \hat{v}_0 + \epsilon\hat{v}_1 + \epsilon^2\hat{v}_2 + \cdots, \quad \text{(C 17)}$$

and

$$\boldsymbol{X} \approx \boldsymbol{X}_0 + \epsilon\boldsymbol{X}_1 + \epsilon^2\boldsymbol{X}_2 + \cdots, \quad \boldsymbol{Y} \approx \boldsymbol{Y}_0 + \epsilon\boldsymbol{Y}_1 + \epsilon^2\boldsymbol{Y}_2 + \cdots, \quad \text{(C 18)}$$

The leading terms of the equations (C 14)–(C 16) then consist of

$$\hat{s}_0 = 0, \quad \text{(C 19)}$$

$$\boldsymbol{X}_0\hat{s}_0 - (1-\boldsymbol{X}_0)\hat{d}_0 + 2\Gamma\hat{v}_0 = 0, \quad \text{(C 20)}$$

$$\boldsymbol{Y}_0\hat{s}_0 + \boldsymbol{Y}_0\hat{d}_0 + \hat{v}_0 = 0. \quad \text{(C 21)}$$

This equation system yields the following dispersion relation:

$$(\boldsymbol{X}_0 - 1)\hat{d}_0 - 2\Gamma\boldsymbol{Y}_0\hat{d}_0 = 0, \quad \text{(C 22)}$$

$$\hat{s}_0 = 0 \quad \text{and} \quad \hat{v}_0 = -\boldsymbol{Y}_0\hat{d}_0. \quad \text{(C 23)}$$

Now, the second lowest terms of the acoustic mode provide $O(\epsilon)$, which is smaller than the second lowest terms of the vorticity or entropy modes ($= O(\epsilon^{1/2})$). Accordingly, the rest of the terms in the acoustic mode (associated with viscous and heat conduction effects) are ignored here. As a result, the following conditions are satisfied:

$$\Delta\hat{d} + 2\frac{k_x \partial U_x/\partial y}{\Omega}\frac{\partial}{\partial y}\hat{d} + \frac{\Omega^2}{a^2}\hat{d} \approx 0, \quad \text{(C 24)}$$

$$\hat{s}^{ac} \approx 0, \quad \hat{T}^{ac} \sim \frac{\hat{p}^{ac}}{\rho C_p}, \quad \hat{u}_y^{ac} \approx -\mathrm{i}\frac{1}{\Omega\rho}\frac{\partial \hat{p}^{ac}}{\partial y}. \quad \text{(C 25)}$$

In fact, (C 24) is identical to the third-order wave operator shown in (2.2).

On the other hand, to derive the relationships for the vorticity and entropy modes, each term must be expanded in terms of $\epsilon^{1/2}$: $\hat{s} \approx \hat{s}_0 + \epsilon^{1/2}\hat{s}_1 + \epsilon\hat{s}_2 + \cdots$; $\boldsymbol{X} \approx \epsilon^{-1}\boldsymbol{X}_0 + \epsilon^{-1/2}\boldsymbol{X}_1 + \boldsymbol{X}_2 + \cdots$; $\boldsymbol{Y} \approx \epsilon^{-1/2}\boldsymbol{Y}_0 + \boldsymbol{Y}_1 + \epsilon^{1/2}\boldsymbol{Y}_2 + \cdots$; and so on. The leading terms yield

$$[1 + \gamma(\epsilon_\kappa/\epsilon)\boldsymbol{X}_0]\hat{s}_0 + (\gamma - 1)(\epsilon_\kappa/\epsilon)\boldsymbol{X}_0\hat{d}_0 + 2(\epsilon_\mu/\epsilon)\Gamma\chi^{-1}\boldsymbol{X}_0\hat{v}_0 = 0, \tag{C 26}$$

$$\boldsymbol{X}_0\hat{s}_0 + \boldsymbol{X}_0\hat{d}_0 = 0, \tag{C 27}$$

$$\boldsymbol{Y}_0\hat{s}_0 + \boldsymbol{Y}_0\hat{d}_0 = 0. \tag{C 28}$$

As observed in a quiescent flow, the solution corresponding to the vorticity mode is $\hat{s}_0 + \hat{d}_0 = 0$; hence, $[1 + (\epsilon_\kappa/\epsilon)\boldsymbol{X}_0]\hat{d}_0 = 2(\epsilon_\mu/\epsilon)\Gamma\chi^{-1}\boldsymbol{X}_0\hat{v}_0$, while the solution to the entropy mode is $\hat{s}_0 + \hat{d}_0 = 0$, $\hat{v}_0 = 0$, and $\boldsymbol{X}_0 = -\epsilon/\epsilon_\kappa$. Subsequently, the second lowest terms in the vorticity mode consist of

$$\begin{aligned}[1 + \gamma(\epsilon_\kappa/\epsilon)\boldsymbol{X}_0]\hat{s}_1 + (\gamma - 1)(\epsilon_\kappa/\epsilon)\boldsymbol{X}_0\hat{d}_1 + [-(\epsilon_\kappa/\epsilon)\boldsymbol{X}_1 + 2(\epsilon_\mu/\epsilon)\Gamma\chi^{-1}\boldsymbol{Y}_0]\hat{d}_0 \\ +2(\epsilon_\mu/\epsilon)\Gamma\chi^{-1}\boldsymbol{X}_0\hat{v}_1 + 2(\epsilon_\mu/\epsilon)\Gamma\chi^{-1}\boldsymbol{X}_1\hat{v}_0 = 0,\end{aligned} \tag{C 29}$$

$$\boldsymbol{X}_0\hat{s}_1 + \boldsymbol{X}_0\hat{d}_1 = 0, \tag{C 30}$$

$$\boldsymbol{Y}_0\hat{s}_1 + \boldsymbol{Y}_0\hat{d}_1 + [1 + (\epsilon_\mu/\epsilon)\boldsymbol{X}_0]\hat{v}_0 = 0. \tag{C 31}$$

Hence, (C 30) and (C 31) derive $\hat{s}_1 + \hat{d}_1 = 0$ and $\boldsymbol{X}_0 = -\epsilon/\epsilon_\mu$. As a result, the leading order in the vorticity mode yields

$$\hat{s}_0 + \hat{d}_0 = 0, \quad [1 - (\epsilon_\kappa/\epsilon_\mu)]\hat{d}_0 + 2\Gamma\chi^{-1}\hat{v}_0 = 0. \tag{C 32}$$

They can be rewritten using the physical quantities as follows:

$$\hat{p}^{vor} \approx 0, \quad \hat{T}^{vor} \approx \mathrm{i}\frac{T}{\Omega}(\nabla \cdot \hat{\boldsymbol{u}}^{vor}) \approx \mathrm{i}\frac{T}{a}\Lambda\hat{u}_y^{vor}, \tag{C 33}$$

where

$$\Lambda = \frac{2Pr}{1 - Pr}\frac{1}{ak_x}\frac{\mathrm{d}U_x}{\mathrm{d}y}$$

and $\hat{p}^{vor}$ is obtained from $\hat{s}^{vor} + \hat{d}^{vor} \approx 0$ and continuity.

Similarly, the second lowest terms in the entropy mode consist of

$$(1 - \gamma)\hat{s}_1 - (\gamma - 1)\hat{d}_1 + [-(\epsilon_\kappa/\epsilon)\boldsymbol{X}_1 + 2(\epsilon_\mu/\epsilon)\Gamma\chi^{-1}\boldsymbol{Y}_0]\hat{d}_0 - 2\frac{\epsilon_\mu}{\epsilon_\kappa}\Gamma\chi^{-1}\hat{v}_1 = 0, \tag{C 34}$$

$$-\frac{1}{\epsilon_\kappa}(\hat{s}_1 + \hat{d}_1) = 0, \tag{C 35}$$

$$\boldsymbol{Y}_0\hat{s}_1 + \boldsymbol{Y}_0\hat{d}_1 = 0. \tag{C 36}$$

Hence, (C 35) and (C 36) also give $\hat{s}_1 + \hat{d}_1 = 0$. However, (C 34) gives only $-\epsilon_\kappa\boldsymbol{X}_1\hat{d}_0 + 2\epsilon_\mu\Gamma\chi^{-1}[\boldsymbol{Y}_0\hat{d}_0 - (\epsilon/\epsilon_\kappa)\hat{v}_1] = 0$. Notice that $\hat{v}_1$ appears to be the leading order despite $\hat{v}_0 = 0$. Expanding further higher terms for the entropy mode to close the leading order, one can eventually obtain $\hat{v}_1 = (\epsilon_\kappa/\epsilon)\boldsymbol{Y}_0\hat{d}_0$; consequently, the effective leading order yields

$$\hat{s}_0 + \hat{d}_0 = 0, \quad (\epsilon_\kappa/\epsilon)\boldsymbol{Y}_0\hat{d}_0 - \hat{v}_1 = 0. \tag{C 37}$$

Likewise, the conditions of the entropy mode can be expressed by

$$\hat{p}^{ent} \approx 0, \quad \hat{T}^{ent} \approx \mathrm{i}\frac{T}{\Omega}(\nabla \cdot \hat{\boldsymbol{u}}^{ent}), \quad \hat{u}_y^{ent} \approx \frac{\kappa}{\rho C_p T}\frac{\partial \hat{T}^{ent}}{\partial y}. \tag{C 38}$$

Comparing the solutions at the leading order between a quiescent and a shear flow, one can notice that a temperature disturbance as well as that of entropy are invoked in the vorticity mode. In addition, the dispersion relation of the acoustic mode changes to the convective wave operator. On the other hand, the entropy mode remains the same.

To further simplify these relations, use the following approximation. Knowing $\boldsymbol{Y} = O(\epsilon^{-1/2})$, the orders of the transverse and horizontal derivatives in the vorticity and entropy modes can be estimated as follows:

$$\frac{\partial}{\partial y} \sim \frac{\Omega}{a}\epsilon^{-1/2} \gg \frac{\Omega}{a} \sim \frac{\partial}{\partial x}. \tag{C 39}$$

Therefore, the $\partial^2/\partial x^2$ term included in $\boldsymbol{X}$ $(= -(a^2/\Omega^2)\Delta)$ can be ignored. As shown in Pierce (1989), define the characteristic length scales of the vorticity and entropy modes as $l_{vor} \equiv \sqrt{2\mu/\omega\rho}$ and $l_{ent} \equiv \sqrt{2\kappa/\omega\rho C_p}$ $(= l_{vor}/Pr^{1/2})$, respectively. Consequently, the dispersion relation of each mode can be replaced by the following transverse derivative:

$$\left(\frac{\partial}{\partial y}\right)^{vor} \approx -(1-\mathrm{i})/l_{vor}, \quad \left(\frac{\partial}{\partial y}\right)^{ent} \approx -(1-\mathrm{i})/l_{ent}. \tag{C 40}$$

Now, the boundary conditions for a non-slip wall and an isothermal or adiabatic wall are expressed as

$$\hat{\boldsymbol{u}}^{ac} + \hat{\boldsymbol{u}}^{vor} + \hat{\boldsymbol{u}}^{ent} = 0, \tag{C 41}$$

$$\hat{T}^{ac} + \hat{T}^{vor} + \hat{T}^{ent} = 0, \quad \text{or} \quad \frac{\partial \hat{T}^{ac}}{\partial y} + \frac{\partial \hat{T}^{vor}}{\partial y} + \frac{\partial \hat{T}^{ent}}{\partial y} = 0. \tag{C 42}$$

Assuming $|\partial/\partial y| \gg |\partial/\partial x|$, differentiate (C 41) in the horizontal direction; subsequently, substitute (C 33) and (C 38), and simplify it using (C 24), (C 25), and (C 40):

$$\begin{aligned}
&\nabla_{\parallel} \cdot (\hat{\boldsymbol{u}}_{\parallel}^{ac} + \hat{\boldsymbol{u}}_{\parallel}^{vor} + \hat{\boldsymbol{u}}_{\parallel}^{ent}) \\
&\quad \approx -\frac{\partial \hat{u}_y^{ac}}{\partial y} + \mathrm{i}\frac{\Omega}{\rho}\hat{\rho}^{ac} + \left(\frac{1-\mathrm{i}}{l_{vor}}\hat{u}_y^{vor} - \mathrm{i}\frac{\Omega}{T}\hat{T}^{vor}\right) + \left(\frac{1-\mathrm{i}}{l_{vor}}\hat{u}_y^{ent} - \mathrm{i}\frac{\Omega}{T}\hat{T}^{ent}\right) \\
&\quad \approx -\mathrm{i}\frac{1}{\rho\Omega}\left(\frac{k_x}{\Omega}\frac{\partial U_x}{\partial y}\frac{\partial \hat{p}^{ac}}{\partial y} - k_x^2\hat{p}^{ac}\right) - \mathrm{i}\frac{1-\mathrm{i}}{l_{vor}}\left(\frac{a}{\Lambda} + \frac{1+\mathrm{i}}{2}l_{vor}\Omega\right)\frac{\hat{T}^{vor}}{T}.
\end{aligned} \tag{C 43}$$

On the other hand, the vertical component of the velocity becomes

$$\hat{u}_y^{ac} + \hat{u}_y^{vor} + \hat{u}_y^{ent} \approx -\mathrm{i}\frac{1}{\rho\Omega}\frac{\partial \hat{p}^{ac}}{\partial y} - \mathrm{i}\frac{a}{\Lambda}\frac{\hat{T}^{vor}}{T} + \frac{\kappa}{\rho C_p T}\frac{\partial \hat{T}^{ent}}{\partial y}. \tag{C 44}$$

Here, one lower-order term $(O(\epsilon))$ is eliminated. For an adiabatic wall, directly substituting (C 40) into (C 44), combining (C 43) with it, and referring to the definition of $\mathscr{Z}$ in (2.4), the non-dimensional form of the acoustic impedance for an adiabatic wall yields

$$\mathscr{Z}_{(2)}^{adb} \approx -\frac{1-\mathrm{i}}{2}\omega\bar{l}_{vor}\bar{k}_x^2\frac{1+\frac{1}{2}(1+\mathrm{i})\omega\Lambda\bar{l}_{ent}^2/\bar{l}_{vor}}{1+\frac{1}{2}(1+\mathrm{i})\omega\Lambda\bar{l}_{vor}(1-[(1-Pr)/2Pr]\bar{k}_x^2)}. \tag{C 45}$$

Likewise, substituting (C 40) into (C 44), the acoustic impedance for an isothermal wall becomes

$$\mathscr{Z}^{ist}_{(2)} \approx -\frac{1-\mathrm{i}}{2}\omega\frac{(\gamma-1)\bar{l}_{ent}(1+\frac{1}{2}(1+\mathrm{i})\omega\Lambda\bar{l}_{vor})+\bar{l}_{vor}\bar{k}_x^2(1+\frac{1}{2}(1+\mathrm{i})\omega\Lambda\bar{l}_{ent})}{1+\frac{1}{2}(1+\mathrm{i})\omega(\bar{l}_{vor}/\bar{k}_x)([2Pr/(1-Pr)-\bar{k}_x^2)(\mathrm{d}M/\mathrm{d}y)_{wall}}. \quad (\mathrm{C}\,46)$$

Here, the superscripts *adb* and *ist* denote adiabatic and isothermal, respectively. Remember that the acoustic wavelength λ is chosen to be the length scale and the speed of sound a to be the velocity scale to non-dimensionalize the expressions above. Hence, for example,

$$\bar{l}_{vor}=\sqrt{\frac{M_\infty}{\pi Re_{ac}}},\quad \bar{l}_{ent}=\sqrt{\frac{M_\infty}{\pi PrRe_{ac}}},\quad \Lambda=\frac{2Pr}{1-Pr}\frac{1}{\omega\bar{k}_x}\left(\frac{\mathrm{d}M}{\mathrm{d}y}\right)_{wall},$$

and so on. (Also note that $\bar{k}_x=\omega k_x$ where $\omega=2\pi$.) In these final results, Ω is replaced by ω since the mean velocity on the wall is zero. As expected, when the Reynolds number increases, the length scales, $\hat{l}_{vor}$ and $\hat{l}_{ent}$, become shorter; subsequently, the acoustic impedance $\mathscr{Z}$ decreases. In particular, the shear flow correction terms Λ (and $(1/\bar{k}_x)(\mathrm{d}M/\mathrm{d}y)_{wall}$) become fairly small at moderate Reynolds numbers; hence, the acoustic impedance is almost the same as that in a quiescent case. One also notices that the acoustic impedance depends on the angle of plane waves, namely the position of the observer. The corresponding observer angles in the far field are given by (2.8) or (2.10) and (2.11). To compare the theoretical predictions for direct waves with the results of DNS, the impedance for the adiabatic wall (C 45) was used for the analytic predictions.

In three dimensions the energy equation corresponding to (C 4), accordingly, (C 7) becomes more complicated. Hence, the modification of (C 45) or (C 46) may not be straightforward. Nonetheless, at the leading order they should become

$$\mathscr{Z}^{adb}_{(3)} \sim -\frac{1-\mathrm{i}}{2}\omega\bar{l}_{vor}(\bar{k}_x^2+\bar{k}_z^2), \quad (\mathrm{C}\,47)$$

$$\mathscr{Z}^{ist}_{(3)} \sim -\frac{1-\mathrm{i}}{2}\omega[(\gamma-1)\bar{l}_{ent}+\bar{l}_{vor}(\bar{k}_x^2+\bar{k}_z^2)]. \quad (\mathrm{C}\,48)$$

These expressions, however, do not include the shear correction terms retained in (C 45) and (C 46).

Appendix D. Viscous dissipation in a uniform flow

Since the Reynolds numbers are not sufficiently high in the DNS, viscous corrections are included in comparing the DNS results with the asymptotic Green's functions for direct waves. Assuming that the energy dissipation mainly occurs in the free stream and the observer positions are far enough away so that the plane wave approximation is valid, a method to correct the viscous dissipation (refer to Pierce 1989, for example) is reviewed.

Starting with the full Navier–Stokes equations, assume the mean velocity U_∞ to be constant, and neglect all nonlinear terms. Consequently, the non-dimensional form of the second-order convective wave equation retaining the viscous and heat conduction terms can be written as

$$\frac{\mathrm{D}^2\Pi}{\mathrm{D}t^2}-\frac{\partial^2\Pi}{\partial x_j^2}=\frac{M_\infty}{Re}\left(\frac{4}{3}+\frac{\gamma-1}{Pr}\right)\frac{\mathrm{D}^3\Pi}{\mathrm{D}t^3}, \quad (\mathrm{D}\,1)$$

where $M_\infty \equiv U_\infty/a_\infty$, $Re \equiv U_\infty\lambda/\nu_\infty$, and $Pr \equiv \mu_\infty Cp/\kappa_\infty$. Here, the right-hand

side is implicitly assumed one order smaller; hence, all dependent variables satisfy $\mathrm{D}^2 f/\mathrm{D}t^2 - \partial^2 f/\partial x_j^2 = 0$ at the leading order. Now, decompose the dependent variable into the Fourier modes; namely, $\Pi \sim \exp[-\mathrm{i}\omega(t - \bar{k}_x x - \bar{k}_y y)]$. Equation (D 1) can be then expressed by

$$-(1 - \bar{k}_x M_\infty)^2 + \bar{k}_x^2 + \bar{k}_y^2 = \mathrm{i}\epsilon_v \omega (1 - \bar{k}_x M_\infty)^3. \tag{D 2}$$

Here

$$\epsilon_v \equiv \frac{M_\infty}{Re}\left(\frac{4}{3} + \frac{\gamma - 1}{Pr}\right),$$

where $\epsilon_v \ll 1$. By asymptotically solving this dispersion equation, the following solution can be found:

$$\bar{k}_x \approx \frac{-M_\infty \pm \sqrt{1 - (1 - M_\infty^2)\bar{k}_y^2}}{1 - M_\infty^2} \pm \mathrm{i}\frac{\epsilon_v}{4}\frac{\omega(1 - \bar{k}_x M_\infty)^3}{\sqrt{1 - (1 - M_\infty^2)\bar{k}_y^2}} \quad (x \gtrless 0) \tag{D 3a}$$

$$\bar{k}_y \approx \sqrt{(1 - \bar{k}_x M_\infty)^2 - \bar{k}_x^2} + \mathrm{i}\frac{\epsilon_v}{4}\frac{\omega(1 - \bar{k}_x M_\infty)^3}{\sqrt{(1 - \bar{k}_x M_\infty)^2 - \bar{k}_x^2}}. \tag{D 3b}$$

One can see that the second terms of both wavenumbers cause exponential decay, which contribute to viscous dissipation. Therefore, the pressure amplitude decay can be expressed by

$$\Pi_{(2)}(t, x, y) \approx \exp\left[-\frac{\epsilon_v \omega^2 (1 - \bar{k}_x M_\infty)^3}{4}\left(\frac{|x|}{\sqrt{1 - (1 - M_\infty^2)\bar{k}_y^2}} + \frac{y}{\bar{k}_y}\right)\right] G_{(2)}(x, y)\, \mathrm{e}^{-\mathrm{i}\omega t}. \tag{D 4}$$

Here, using the expression for the stationary point in (2.8) and comparing it with the leading order of (D 2), one can derive $\bar{k}_y \sim \sin\phi/\sqrt{1 - M_\infty^2 \sin^2\phi}$. Thus, the formula (D 4) is included when Green's functions for direct waves are evaluated.

Appendix E. Post-processing to extract channelled waves

To calculate normal modes of channelled waves, the following Riccati forms of the third-order convective wave operator and its adjoint operator were solved by the standard fourth-order Runge–Kutta scheme based on a steady laminar boundary layer velocity profile obtained from DNS at $x = 0$ (see figure 28 for the overall procedures for the data processing):

$$\frac{\mathrm{d}Q}{\mathrm{d}y} + \left(Q + \frac{2k_x \mathrm{d}M/\mathrm{d}y}{\omega - k_x M}\right) Q + (n^2 - k_x^2) = 0, \tag{E 1}$$

and

$$\frac{\mathrm{d}Q^\dagger}{\mathrm{d}y} + \left(Q^\dagger - \frac{4k_x \mathrm{d}M/\mathrm{d}y}{\omega - k_x M}\right) Q^\dagger + \left(n^2 - k_x^2 - \frac{3k_x \mathrm{d}^2 M/\mathrm{d}y^2}{\omega - k_x M}\right) = 0, \tag{E 2}$$

with the boundary conditions given by

$$Q(0) = 0, \quad Q(\infty) = -\sqrt{n_\infty^2 - k_x^2}, \tag{E 3}$$

and

$$Q^\dagger(0) = 3\frac{k_x}{\omega}\frac{\mathrm{d}M}{\mathrm{d}y}\bigg|_{y=0}, \quad Q^\dagger(\infty) = -\sqrt{n_\infty^2 - k_x^2}, \tag{E 4}$$

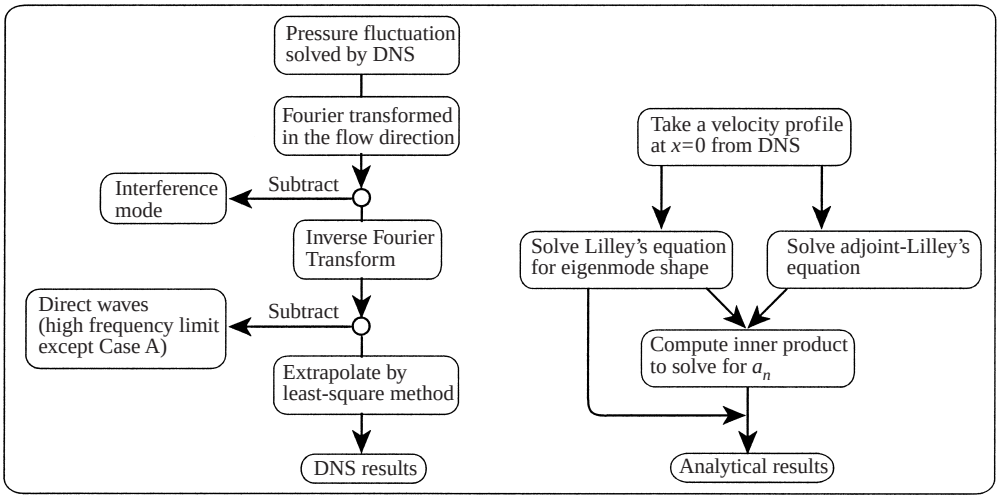

FIGURE 28. Flow chart of the date processing to compare channelled waves between the theoretical predictions and the DNS results.

where $Q(y) = A'(y)/A(y)$ and $Q^\dagger(y) = A^{\dagger\prime}(y)/A^\dagger(y)$. Equations (E 1) and (E 2) were both integrated from $y = 0$ and $y = y_{max}$ to the turning point by a shooting method, and the wavenumbers k_{xm} were computed by the Newton method. (A similar procedure was used to compute k_{xm} for diffracted waves using the Newton–Raphson method.) To calculate the inner products (2.33), the trapezoidal rule (second order) was used, and the width of the source in the y-direction was taken into account in the numerical integration.

In the DNS the eigenmode shapes of channelled waves near the wall show some changes in the x-direction due to the viscous dissipation and the interference with direct waves in the free-stream (see figure 29). Therefore, to compare the DNS results with the theoretical predictions, eigenmode shapes were calculated as follows. Refer to figure 28 for the procedures. (Note that only the low-frequency case, Case A, was processed by simply taking an average in the x-direction and eliminating the contribution from direct waves due to the fact that the interference pattern was longer than the computational domain.) First, the inviscid solutions were considered. Referring to (2.16), the pressure fluctuation was assumed to be

$$\hat{G}_{(2)}(\boldsymbol{x}|\omega, 0, \eta) = \sum_{m=1}^{N} A_m(y)\cos(\omega t - k_{xm}x - \alpha_m). \tag{E 5}$$

Here, A_m includes eigenfunctions of direct waves as well as channelled waves. Although direct waves should have continuous spectrum, it can be approximated by discrete modes due to the fact that the dominant wavenumber is given by the stationary phase method, namely (2.8). To take a discrete Fourier transform in time, the following quantities were computed using the DNS data:

$$\begin{aligned}\hat{G}^{cos}_{(2)}(x, y) &\equiv \frac{2}{N_{ft}} \sum_{j=1}^{N_{ft}} \cos\omega t_j \sum_{m=1}^{N} A_m(y)\cos(\omega t_j - k_{xm}x - \alpha_m) \\ &\approx \sum_{m=1}^{N} A_m(y)\cos(k_{xm}x + \alpha_m),\end{aligned} \tag{E 6}$$

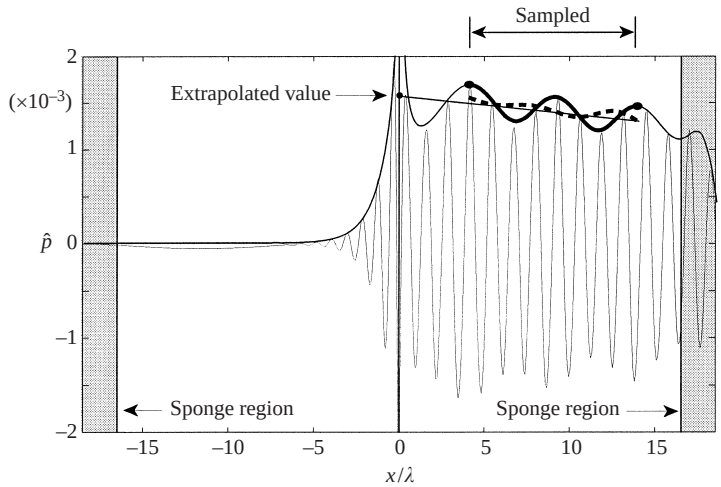

FIGURE 29. Viscous decay of channelled waves in Case B. Instantaneous pressure profile and its amplitude taken by the Fourier transform along $y = \eta$ are shown. The thick solid line within the sampled interval denotes the original profile, and the thick dashed line denotes the profile excluding the interference mode. The thin line denotes the least-square approximation after the direct wave contribution is eliminated. (It is not a straight line in this figure because the line is defined in the pressure square domain.)

$$\hat{G}^{sin}_{(2)}(x,y) \equiv \frac{2}{N_{ft}} \sum_{j=1}^{N_{ft}} \sin \omega t_j \sum_{m=1}^{N} A_m(y) \cos(\omega t_j - k_{xm} x - \alpha_m)$$
$$\approx \sum_{m=1}^{N} A_m(y) \sin(k_{xm} x + \alpha_m). \tag{E 7}$$

In this study, N_{ft} was chosen to be $= 2^n$, where $n \in \mathbf{N}$, and the sample time was set to be an exact multiple of the period at the forcing frequency with equal time intervals so that the second equalities of (E 6) and (E 7) were exact. Consequently, the square of the amplitude field was calculated as

$$|\hat{G}_{(2)}|^2 \equiv |\hat{G}^{cos}_{(2)}|^2 + |\hat{G}^{sin}_{(2)}|^2 = \sum_{m=1}^{N} A_m^2(y)$$
$$+ \sum_{m_1 \neq m_2}^{N} 2A_{m_1}(y) A_{m_2}(y) \cos[(k_{xm_1} - k_{xm_2})x + (\alpha_{m_1} - \alpha_{m_2})]. \tag{E 8}$$

Here, the second summation corresponds to the interference part. Among these terms, it was assumed that the interference between the normal mode of the channelled waves (with a purely real k_x) and that of the direct waves in the free stream is by far the largest; accordingly, only three terms survive in (E 8): two auto-correlations and one cross-correlation of the direct waves and the channelled waves. Next, by observing the distribution of (E 8) at $y = \eta$ based on the DNS data, an appropriate spatial interval for sampling was chosen so that the interference mode was distinguished well (see figure 29). Subsequently, this profile was converted to the wavenumber space by a discrete Fourier transform in the x-direction, a mode corresponding to the interference was eliminated, and the date was recovered by an inverse Fourier transform. Assuming the resultant distribution only retains the auto-correlations of (E 8), the contribution

from the direct waves was eliminated based on the high-frequency asymptotic formula (2.14) (only for Case A, the low-frequency asymptotic formula (2.7) was used). Finally, the eigenmode shapes were extrapolated to $x = 0$ based on the least-square method to recover the viscous dissipation. When the amplitude square was evaluated to be negative; namely the contribution from the direct waves was over-estimated, it was depicted by • as shown in figure 22. Strictly speaking, direct waves algebraically fall off, while the viscous dissipation provides exponential decay. But, assuming these effects to be relatively small, they were linearly approximated. This process was repeated for each y, and the normal mode shape at $x = 0$ was calculated.

REFERENCES

Abrahams, I. D. & Kriegsmann, G. A. 1994 Sound radiation and caustic formation from a point source in a wall shear layer. *AIAA J.* **32**, 1135–1144.

Abramowitz, M. & Stegun, I. 1965 *Handbook of Mathematical Functions with Formulas, Graphs, and Mathematical Tables*. Dover.

Ahluwalia, D. S. & Keller, J. B. 1977 Exact and asymptotic representations of the sound field in a stratified ocean. In *Wave Propagation and Underwater Acoustics* (ed. J. B. Keller & J. S. Papadakis). Lecture Notes in Physics, vol. 70, pp. 14–84. Springer.

Anderson, M. J. & Vaidya, P. G. 1991 Thermo-viscous effects on finite amplitude sound propagation in a rectangular waveguide. *J. Acoust. Soc. Am.* **90**, 1056–1067.

Avila, G. S. S. & Keller, J. B. 1963 The high-frequency asymptotic field of a point source in an inhomogeneous medium. *Commun. Pure Appl. Maths* **16**, 363–381.

Balsa, T. F. 1976 The far field of high-frequency convected singularities in sheared flows, with an application to jet-noise prediction. *J. Fluid Mech.* **74**, 193–208.

Beckemeyer, R. J. 1974 Application of an inner expansion method of plane, inviscid, compressible flow stability studies. *J. Fluid Mech.* **62**, 405–416.

Brekhovskikh, L. & Lysanov, Y. 1982 In *Fundamentals of Ocean Acoustics*, pp. 109–138. Springer.

Coleman, G. N., Kim, J. & Moser, R. D. 1995 A numerical study of turbulent supersonic isothermal-wall channel flow. *J. Fluid Mech.* **305**, 159–183.

Curle, N. 1955 The influence of solid boundaries upon aerodynamic sound. *Proc. R. Soc. Lond.* A **231**, 505–514.

Durbin, P. A. 1983 High frequency Green's function for aerodynamic noise in moving media, Part I: General theory. *J. Sound Vib.* **91**, no. 4, 519–525.

Ffowcs Williams, J. E. & Hall, L. H. 1970 Aerodynamic sound generation by turbulent flow in the vicinity of a scattering half plane. *J. Fluid Mech.* **40**, 657–670.

Ffowcs Williams, J. E. & Purshouse, M. 1981 A vortex sheet modelling of boundary-layer noise. *J. Fluid Mech.* **113**, 187–220.

Freund, J. B. 1997 Proposed inflow/outflow boundary condition for direct computation of aerodynamic sound. *AIAA J.* **35**, 740–742.

Giles, M. B. 1990 Nonreflecting boundary conditions for Euler equation calculations. *AIAA J.* **28**, 2050–2058.

Goldstein, M. E. 1978 Characteristics of the unsteady motion on transversely sheared mean flows. *J. Fluid Mech.* **84**, 305–329.

Goldstein, M. E. 1982 High frequency sound emission from moving point multipole sources embedded in arbitrary transversely sheared mean flows. *J. Sound Vib.* **80**, 499–522.

Goldstein, M. E. & Leib, S. J. 2000 Emission of sound from turbulence convected by a parallel mean flow in the presence of a confining duct. *J. Sound Vib.* **235**, no.1 25–42.

Graham, W. R. 1996 Boundary layer induced noise in aircraft, Part I: The flat plate model. *J. Sound Vib.* **192**, 101–120.

Howe, M. S. 1979 The role of surface shear stress fluctuations in the generation of boundary layer noise. *J. Sound Vib.* **65**, 159–164.

Howe, M. S. & Shah, P. L. 1996 Influence of mean flow on boundary layer generated interior noise. *J. Acoust. Soc. Am.* **99**, 3401–3411.

KIRCHHOFF, G. 1868 Ueber den Einflußs der Wärmeleitung in einem Gase auf die Schallbewegung. *Annal. Physik Chemie* **134**, 177–193.

KRIEGSMANN, G. A. & REISS, E. L. 1983 Acoustic propagation in wall shear flows and the formation of caustics. *J. Acoust. Soc. Am.* **74**, 1869–1879.

LELE, S. K. 1992 Compact finite difference schemes with spectral-like resolution. *J. Comput. Phys.* **103**, 16–42.

LIGHTHILL, M. J. 1952 On sound generated aerodynamically: I. General theory. *Proc. R. Soc. Lond.* A **211**, 564–587.

LILLEY, G. M. 1974 On the noise from jet. *AGARD* **131**, 1–12. (Report number): CP131.

MACK, L. M. 1984 Remarks on disputed numerical results in compressible boundary-layer stability theory. *Phys. Fluids* **27**, 342–347.

MANI, R. 1980 Sound propagation in parallel sheared flows in ducts: the mode estimation problem. *Proc. R. Soc. Lond.* A **371**, 393–412.

MÖHRING, W., MÜLLER, E. A. & OBERMEIER, F. 1983 Problems in flow acoustics. *Rev. Mod. Phys.* **50**, 707–724.

PIERCE, A. D. 1989 *Acoustics: An Introduction to its Physical Principles and Applications.* The Acoustic Society of America.

POWELL, A. 1960 Aerodynamic noise and the plane boundary. *J. Acoust. Soc. Am.* **32**, 982–990.

POWELL, A. 1991 Nature of the sound sources in low-speed jet impingement. *J. Acoust. Soc. Am.* **90**, 3326–3331.

PRIDMORE-BROWN, D. C. 1958 Sound propagation in a fluid flowing through an attenuating duct. *J. Fluid Mech.* **4**, 393–406.

RAMAKRISHNAN, R. 1980 Radiation in a wall jet flow environment. *J. Sound Vib.* **68**, 389–405.

SALWEN, H. &. GROSCH, C. E. 1981 The continuous spectrum of the Orr–Sommerfeld equation. Part 2. Eigenfunction expansions. *J. Fluid Mech.* **104**, 445–465.

SECKLER, B. D. & KELLER, J. B. 1959*a* Geometrical theory of diffraction in inhomogeneous media. *J. Acoust. Soc. Am.* **31**, 192–205.

SECKLER, B. D. & KELLER, J. B. 1959*b* Asymptotic theory of diffraction in inhomogeneous media. *J. Acoust. Soc. Am.* **31**, 206–216.

SHEN, J. & MEECHAM, W. C. 1993 Quadrupole directivity of jet noise when impinging on a large rigid plate. *J. Acoust. Soc. Am.* **94**, 1415–1424.

SUZUKI, T. 2001 Acoustic wave propagation in transversely sheared flows. PhD thesis, Stanford University, Stanford.

SUZUKI, T. & LELE, S. K. 2003 Green's functions for a source in a mixing layer: direct waves, refracted arrival waves and instability waves. *J. Fluid Mech.* **477**, 89–128 (referred to herein as Part 1).

SWINBANKS, M. A. 1975 The sound field generated by a source distribution in a long duct carrying sheared flow. *J. Sound Vib.* **40**, 51–76.

WANG, M. & KASSOY, D. R. 1992 Transition acoustic processes in a low-Mach-number shear flow. *J. Fluid Mech.* **238**, 509–536.

WILBY, J. F. 1996 Aircraft interior noise. *J. Sound Vib.* **190**, 545–564.